UCRL-JRNL-212909

LAWRENCE
LIVERMORE
NATIONAL
LABORATORY

FIRST-PRINCIPLES APPROACHES TO THE STRUCTURE AND REACTIVITY OF ATMOSPHERICALLY RELEVANT AQUESOUS INTERFACES

C. Mundy, I-F. W. Kuo

June 14, 2005

CHEMICAL REVIEWS

This document was prepared as an account of work sponsored by an agency of the United States Government. Neither the United States Government nor the University of California nor any of their employees, makes any warranty, express or implied, or assumes any legal liability or responsibility for the accuracy, completeness, or usefulness of any information, apparatus, product, or process disclosed, or represents that its use would not infringe privately owned rights. Reference herein to any specific commercial product, process, or service by trade name, trademark, manufacturer, or otherwise, does not necessarily constitute or imply its endorsement, recommendation, or favoring by the United States Government or the University of California. The views and opinions of authors expressed herein do not necessarily state or reflect those of the United States Government or the University of California, and shall not be used for advertising or product endorsement purposes.

Updated October 14, 2003

First-Principles Approaches to the Structure and Reactivity of Atmospherically Relevant Aqueous Interfaces

Christopher J. Mundy[*] *and I-Feng W. Kuo*

Computational Chemical biology
Chemistry and Materials Science
Lawrence Livermore National Laboratory
PO Box 808, Livermore CA, 94551

SUBMISSION DATE: June 9, 2005

[*]Corresponding author, Email: mundy2@llnl.gov

1 Introduction 3
2 Methods 5
2.1 Plane-wave approach 7
2.2 Hybrid methods 10
2.3 Boundary conditions 13
3 Spectroscopic observables 16
3.1 Infrared 17
3.2 Raman 19
3.3 X-ray 20
4 Solid-vapor interfaces 21
4.1 Ice 24
4.2 Nitric Acid Tri-hydrate 32
5 Liquid-vapor interfaces 34
6 Future prospects and applications 43
6.1 Metadynamics 44
7 Acknowledgments 46
8 References 47

1 Introduction

The field of atmospheric science is very rich in problems ranging from the molecular to the regional and global scale. These problems are often extremely complex, and although the statement of a particular atmospheric science question may be clear, finding a single, concise computational approach to address this question can be daunting. As a result, the broad scope of scientific problems that lie within the umbrella of atmospheric science require a multi-discipline approach. Of particular interest to atmospheric chemists is the role that heterogeneous chemistry plays in the important processes that take place throughout the atmosphere. The definition of heterogeneous is: *consisting of dissimilar elements or parts*. The chemical environment induced by the presence of the interface can be dramatically different than the corresponding gas- or condensed phase *homogeneous* environment and can give rise to novel chemistry[12,13]. Although the importance of heterogeneous chemistry in the atmosphere has been known for decades [11,16], a challenge to both experimentalists and theorists in provide simplified models and experiments that can yield insight into the field measurements of the atmospheric process. The use of molecular modeling has been widely used to provide a particle-based picture of atmospherically relevant interfaces to deduce the novel chemistry that is taking place. Unfortunately, even with the most computationally efficient particle-based approach, it is still impossible to model the full ice-crystal in the stratosphere or the sea-salt aerosol in the troposphere. Figure 1

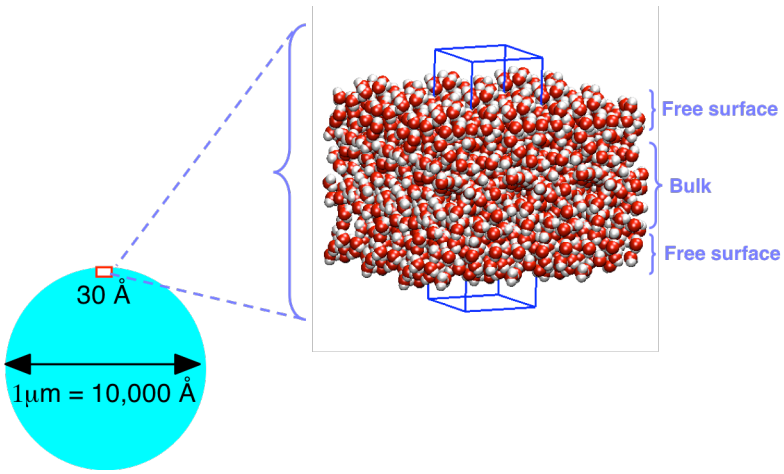

Figure 1: A cartoon depicting the approximations leading to a semi-infinite slab that need to be employed when modeling an aerosol (depicted in aqua) via molecular modeling. Note that the atomistic model of a water interface (oxygen in red, hydrogen in white) of the un-replicated supercell, (in blue), is considered a small enough region to be approximately flat. This model also introduces two free interfaces.

depicts a caricature of the actual system of interest, and highlights the region where efficient molecular modeling can be employed. Although there is seemingly a large disconnect between reality and the model, we hope to convince the reader that there is still much insight to be gained from a particle-based picture.

There is a myriad of different approaches to molecular modeling that have been successfully applied to studying the complex problems put forth by atmospheric chemists. To date, the majority of the molecular models of atmospherically relevant interfaces have been comprised of two genres of molecular models. The first is based on empirical interaction potentials. The use of an empirical interaction potential suffers from at least two shortcomings. First, empirical potentials are usually fit to reproduce bulk thermodynamic states, or gas phase spectroscopic data. Thus, without the explicit inclusion of charge transfer, it is not at all obvious that empirical potentials can faithfully reproduce the structure at a solid-vapor, or liquid-vapor interface where charge rearrangement is known to occur (see section 5). One solution is the empirical inclusion of polarization effects[4,8,10,17]. These models are certainly an improvement, but still cannot offer insight into charge transfer processes and are usually difficult to parameterize. The other shortcoming of empirical models is that, in general, they cannot describe bond-making/breaking events, *i.e.* chemistry.

In order to address chemistry one has to consider an *ab initio* (to be referred to as first-principles throughout the remaining text) approach to molecular modeling that explicitly treats the electronic degrees of freedom. First-principles modeling also give a direct link to spectroscopic data and chemistry, but at a large computational cost. The bottle-neck associated with first-principles modeling is usually determined by the level of electronic structure theory that one chooses to study a particular problem. High-level first-principles approaches, such as MP2, provide accurate representation of the electronic degrees of freedom but are only computationally tractable when applied to small system sizes (*i.e.* 10s of atoms). Nevertheless, this type of modeling has been extremely useful in deducing reaction mechanisms of atmospherically relevant chemistry that will be discussed in this review (see section 4).

However, to solve problems relating to heterogeneous chemistry at interfaces where the interfacial system is large enough to include the effects of the semi-infinite system (see Figure 1), dramatically reduces the number of electronic structure methods available.

Due to the limitation of space and focus, only the first-principles methods that can be utilized to treat the semi-infinite interfacial system, shown in Figure 1, will be discussed. One method that provides a compromise between accuracy and computational efficiency is the Kohn-Sham (KS) formulation of density functional theory (DFT) which will be discussed in section 2. Here, we will review both static and dynamic first-principles methods reviewed that provide a direct link to the heterogeneous chemistry that takes place in the troposphere and stratosphere. Within the development of the theory in section 2, we will discuss two complementary approaches to the modeling of interfacial systems, discuss the state-of-the-art, first-principles simulation protocol for ensuring accurate results for these complicated interfacial systems. Section 3 will focus on the spectroscopic observables that can be directly computed from a first-principles simulation and are relevant to elucidating aqueous systems. Sections 4-5 will highlight some of the recent work on heterogeneous chemistry on solid-vapor and liquid-vapor interfaces. Last, in section 6 we will also highlight the powerful, new methodological developments that will hopefully lead the reader to conclude that large-scale first-principles modeling of heterogeneous processes has a bright future.

2 Methods

Although there is no strict simulation protocol for the study of heterogeneous systems using first-principles modeling, in order to obtain experimentally relevant results, there must be a fusion of two components, namely a fast electronic structure methodology and an efficient sampling scheme. Both of the aforementioned attributes have been incorporated within the Car-Parrinello approach (CP)[18] to first-principles (MD) molecular dynamics. The advent of the KS formulation of DFT (KS-DFT) provides the electronic structure framework on which the majority of modern applications to first-principles

molecular dynamics is based[19-21]. The confluence of an orbital-based treatment of the kinetic energy, fused with pure density functional theory[19,20] provides unprecedented computational efficiency over more traditional perturbative methods, at the expense of accuracy[21-23]. Thus, it has been feasible to study bulk materials for the last four decades. The earliest first-principles MD simulations were performed by quenching the electronic structure to the Born-Oppenheimer (BO) surface at every MD step. The subsequent forces on the ions are a sum of those computed via the Hellman-Feynman theorem, and in some cases, Pulay forces[21]. This method of quenching the wave function at every step of a MD simulation is known as BO MD. Although the BO MD is extremely efficient for solids, where the atoms are not significantly diffusing, simulations of liquids via first-principles MD was in need of a more efficient sampling scheme for the electronic degrees of freedom. Furthermore, even with the best wavefunction optimization schemes, one is not able to efficiently converge to machine precision, thus giving rise to an unwanted drift in the conserved quantity[24]. To cut down on computational cost and increase efficiency and stability of first-principles MD simulation, Car and Parrinello introduced a fictitious dynamics of the electronic degrees of freedom to facilitate on-the-fly computation of the electronic structure[18].

This on-the-fly sampling of the electronic degrees of freedom is a natural consequence of using an extended Lagrangian that takes advantage of the time-scale separation between the nuclear and electronic degrees of freedom. Thus, the CP extended Lagrangian can be written as[18,24]

$$L_{CP} = \underbrace{\sum_I \tfrac{1}{2} M_I \dot{R}_I^2 + \sum_i \tfrac{1}{2} \mu_i \langle \dot{\psi}_i | \dot{\psi}_i \rangle}_{\text{Kinetic Energy}} - \underbrace{\langle \Psi_0 | H_e | \Psi_0 \rangle}_{\text{Potential Energy}} + \text{constraints.}$$

Eqn. 1

Here, the potential energy is computed from the electronic Hamiltonian, H_e, which will be defined in section 2.1. The total wavefunction, Ψ_0, is composed of i single particle orbitals, ψ_i, M_I and $\boldsymbol{R}_I$ denote the mass and position of the Ith ion, with the addition of constraints to enforce orthonormality. Kinetic energy for the one particle orbitals is introduced with fictitious mass μ_i. The equations of motion

derived from L_{CP} become

$$M_I \ddot{R}_I(t) = -\frac{\partial}{\partial R_I}\langle \Psi_0 | H_e | \Psi_0 \rangle + \text{constraints}$$

$$\mu_i \ddot{\psi}_i(t) = -\frac{\delta}{\delta \psi_i^*}\langle \Psi_0 | H_e | \Psi_0 \rangle + \text{constraints}$$

Eqn. 2

For clarity, the explicit orthonormality constraints are excluded. The choice of an appropriate fictitious mass, μ_i, will ensure that there is adiabatic separation between the nuclear and the fictitious electronic degrees of freedom[18,24]. The simultaneous integration of the above equations of motion will ensure proper sampling of the electronic degrees of freedom and a faithful representation of the nuclear forces. Because one is no longer dependent on the convergence of the wavefunction to machine precision, a stable, energy conserving MD simulation is obtained[18,24]. It should be pointed out that the choice of fictitious mass μ_i, can have adverse affects on the trajectory if not properly monitored. The protocol for choosing μ_i and its effect on observables has recently been studied in great detail[9,25,26].

Although bulk condensed phase simulation using first-principles MD simulation is a mature field, the use of the aforementioned methodology can be challenging when applied to interfacial systems. In general, one needs larger system sizes to model interfacial systems. In sections 2.1 and 2.2 we will review two efficient implementations of the electronic structure that allow one to perform large-scale studies of interfaces. Both methods have source code that is freely available on the web[27,28]. Not all of the methods that are utilized in this review are based on the efficient solution of the KS-DFT. Periodic Hartree-Fock (HF) software is also available publicly, and can be used to successfully treat interfacial systems, but usually excludes the finite temperature MD[29-31]. Finally, in section 2.3 we will review the state-of-the-art methods in applying the proper boundary conditions necessary to treat heterogeneous systems.

2.1 Plane-wave approach

The KS-DFT as implemented within the framework of CP-MD (and the software package **CPMD**[28,32]) uses a plane-wave basis set to describe both the wavefunction and density. In the simplest form, the Kohn-Sham energy functional can be written as

$$E_{\mathrm{KS}} = E_{\mathrm{kin}}[\psi_i] + E_{\mathrm{ES}}[n(\mathbf{r})] + E_{\mathrm{XC}}[n(\mathbf{r})].$$

Eqn. 3

Here,

$$\begin{aligned}
E_{\mathrm{kin}} &= -\tfrac{1}{2}\int d\mathbf{r}\psi_i \nabla^2 \psi_i \\
E_{\mathrm{ES}} &= E_{\mathrm{H}} - \sum_I \int d\mathbf{r}\, V^I_{\mathrm{core}}(\mathbf{r}) n(\mathbf{r}) + \sum_{I \neq J} \frac{Z_I Z_J}{\mathbf{R}_I - \mathbf{R}_J} \\
E_{\mathrm{H}} &= \int d\mathbf{r}\, d\mathbf{r}' \frac{n(\mathbf{r}')n(\mathbf{r})}{\mathbf{r} - \mathbf{r}'} \\
n(\mathbf{r}) &= \sum_i |\psi_i|^2
\end{aligned}$$

Eqn. 4

where, n is the electronic density, Z is the nuclear charge, $\boldsymbol{R}_I$ denotes the Ith nuclear coordinate, and V^I_{core} is the potential due to the core electrons. In practice, V^I_{core} is treated within the of psuedopotential (PP) approximation[33-35]. Last, the functional form of the exact exchange-correlation (XC) operator E_{XC} is unknown. The first type of approximation used to compute the XC energy is based the local density approximation (LDA)

$$E_{\mathrm{XC}}^{\mathrm{LDA}}\left[n(\mathbf{r})\right] = \int \varepsilon_{\mathrm{XC}}^{\mathrm{LDA}}\left(n(\mathbf{r})\right) n(\mathbf{r}) d\mathbf{r}.$$

Eqn. 5

Here, $\varepsilon_{\mathrm{XC}}\left(n(\mathbf{r})\right)$ is the XC energy per particle interacting with a uniform electron gas[21]. Although XC using LDA has been shown to give useful results for most chemical applications, a more commonly used approximation now to compute the XC is called the generalized gradient approximation (GGA) where

$$E_{XC}^{GGA}\left[n(\mathbf{r})\right] = \int \varepsilon_{XC}^{GGA}\left(n(\mathbf{r}), \nabla n(\mathbf{r})\right) d\mathbf{r}.$$

Eqn. 6

In this formulation, the ε_{XC}^{GGA} is now dependent on both the density, as well as the gradient of the density giving a hint of non-local character[21]. Some popular GGA functionals that may be referred to in this review are BLYP[14,15], PBE[36], HCTCH[37], OLYP[38]. In addition, there are now hybrid XC functionals, such as B3LYP[39], PBE0[40] AND X3LYP[41], that compute the exact exchange term in a similar fashion to HF[24].

Although a variety of basis sets can be used within the CP-MD approach, the systems of interest to early users and developers of CP-MD method were those of periodic condensed phase systems. Thus, the use of the translationally invariant plane-wave expansion is ideal, with no basis set superposition error (BSSE) introduced. The plane-wave expansion for the single particle orbitals takes on the form

$$\psi_i(\mathbf{r}) = \frac{1}{\sqrt{V}} \sum_{\mathbf{G}} c^i_{\mathbf{G}} \exp[i\mathbf{G}\cdot\mathbf{r}]$$

Eqn. 7

where V is the volume of the periodic supercell, $c_{\mathbf{G}}$ is the reciprocal-space coefficient to be optimized, and $\mathbf{G}$ is the reciprocal lattice vector. Thus, the electronic density, $n(\mathbf{r})$ becomes

$$n(\mathbf{r}) = \frac{1}{\sqrt{V}} \sum_{\mathbf{G}} n(\mathbf{G}) \exp[i\mathbf{G}\cdot\mathbf{r}]$$
$$n(\mathbf{G}) = \sum_i \sum_{\mathbf{G}'} c^{i*}_{\mathbf{G}'-\mathbf{G}} c^i_{\mathbf{G}'}$$

Eqn. 8

Given the definition of the orbitals and the density in the plane-wave basis, we are now able to discuss the efficiency of the computational strategy in computing E_{KS}.

In order to obtain the ground state orbitals, and density, we solve the self-consistent field (SCF) problem by zeroing the variations E_{KS} with respect to the set of single particle orbitals, ψ_i, namely

$$\frac{\delta E_{\mathrm{KS}}}{\delta \psi_i^*} = H_{\mathrm{KS}} \psi_i$$

Eqn. 9

where the connection to Eqn. 1 is established with $H_e = H_{\mathrm{KS}}$. Here, H_{KS} is given by

$$
\begin{aligned}
&H_{\mathrm{KS}} = -\tfrac{1}{2}\nabla^2 + V_{\mathrm{KS}}(\mathbf{r}) \\
&V_{\mathrm{KS}}(\mathbf{r}) = V_{\mathrm{H}} + V_{\mathrm{XC}} \\
&V_{\mathrm{H}} = \int d\mathbf{r}' \frac{n_{\mathrm{tot}}(\mathbf{r}')}{\mathbf{r}-\mathbf{r}'}; \quad n_{\mathrm{tot}}(\mathbf{r}) = n\ (\mathbf{r}) + n_{\mathrm{core}}(\mathbf{r}), \\
&V_{\mathrm{XC}} = \frac{\delta E_{\mathrm{XC}}}{\delta n(\mathbf{r})}
\end{aligned}
$$

Eqn. 10

where we assume that the external potential is only due to the bare nuclear charges. There are three main components of a plane-wave calculation: the computation of n, V_{KS}, and the application of V_{KS} to the single particle orbitals, ψ_i. In practice, the calculation of the total energy is done in real-space, namely

$$E_{\mathrm{KS}} = \int d\mathbf{r}\ V_{\mathrm{KS}}(\mathbf{r}) n(\mathbf{r}).$$

Eqn. 11

The computation of the density from the orbitals in reciprocal-space ($c^i_{\mathbf{G}}$) require $\mathrm{N}_{\mathrm{states}}$ fast-Fourier transforms (FFT). Each FFT scales as $O(\mathrm{N}_{\mathrm{grid}} \log \mathrm{N}_{\mathrm{grid}},)$ where $\mathrm{N}_{\mathrm{grid}}$ denotes the number of real-space grid points[42]. The calculation of V_{KS} in real-space requires the calculation of $V_{\mathrm{XC}}(\mathbf{r})$ and $V_{\mathrm{H}}(\mathbf{r})$. $V_{\mathrm{XC}}(\mathbf{r})$ is constructed directly in real-space, whereas $V_{\mathrm{H}}(\mathbf{r})$ is computed via the reciprocal-space density, $n(\mathbf{G})/\mathbf{G}^2 = V_{\mathrm{H}}(\mathbf{G})$ followed by a single FFT. The application of $V_{\mathrm{KS}}(\mathbf{r})$ on ψ_i requires two FFTs for each state. The first transforms $c^i_{\mathbf{G}}$ to ψ_i, followed by the application of $V_{\mathrm{KS}}(\mathbf{r})$, and transforming back to the new $c^i_{\mathbf{G}}$ where the calculation is repeated until self-consistency is achieved.

It should be clear from the above analysis, that although the **CPMD** package is quite efficient, the algorithm necessary to perform an optimization of the wavefunction does not scale linearly with the number of states or real-space grid points (*i.e.* volume). However, as we will find in sections 4-5 that it is still possible to simulate physically relevant interfacial models with varying degrees of computational resources.

2.2 Hybrid methods

As alluded to in section 2.1 the use plane-wave basis set in conjunction with the FFT has made CP-

MD simulations of systems (N_{atom} < 100) routine on modest computational resources. Unfortunately, for systems of interest in this review, such as the simulation of an interface, or even a simple peptide requires much larger system sizes (N_{atom} > 1000) and applications of a plane-wave based CP-MD method become impractical without state-of-the-art capability computing resources (see http://www.top500.org).

In light of this, the new hybrid methods based on using mixed basis such as the Gaussian and plane-wave (GPW) and the Gaussian and augmented plane-wave (GAPW) approaches are emerging and look to be very promising.[9,43-46]. The aforementioned methods make up the QUICKSTEP module in the software suite **CP2K**[27]. In these hybrid approaches, atom centered Gaussian type orbitals (GTO) are used to describe the oribitals, while plane-waves (PW) are used as an auxiliary basis set to describe the electronic density. Within the context of GPW method, the PW expansion and its electronic density representation (denoted $n^{\mathrm{PW}}(\mathbf{r})$ in this section) is similar to those discussed in section 2.1. The electronic density, as described by GTO, can be written as

$$n^{\mathrm{GTO}}(\mathbf{r}) = \sum_{\mu\nu} P^{\mu\nu} \varphi_{\mu}(\mathbf{r}) \varphi_{\nu}(\mathbf{r})$$

Eqn. 12

where $\psi_i(\mathbf{r}) = \sum_{\mu} c_{\mu i} \varphi_{\mu}(\mathbf{r})$ are the single particle orbitals expanded using primitive Gaussian, $\varphi_{\mu}(\mathbf{r})$, variational coefficients $c_{\mu i}$, and the density matrix $P^{\mu\nu} = \sum_{i} c_{\mu i} c^{*}_{\nu i}$. The flow of the GPW calculation is similar to that outlined in section 2.1, namely the calculation of n, V_{KS}, and the application of V_{KS} to the single particle orbitals. The differences lie in the details of the calculations. Because we have a real-space representation of the single-particle orbitals, $\varphi_{\mu}(\mathbf{r})$ the density can be constructed directly in real-space by an efficient collocation of the primitive Gaussians[45]. Thus, the calculation of $n^{\mathrm{GTO}}(\mathbf{r})$ can be made strictly $O(N_{states})$. The calculation of the $V_{KS}(\mathbf{r})$ is identical to that discussed in section 2.1. Because of the choice of plane-waves for the auxiliary basis set, one can construct $n^{\mathrm{PW}}(\mathbf{r})$ with a single

FFT from $n^{\mathrm{GTO}}(\mathbf{r})$, and one proceeds to $V_{\mathrm{H}}(\mathbf{r})$ in an identical fashion as outlined in section 2.1. Thus, the use of a plane-wave auxiliary basis facilitates a $\mathrm{N_{grid}log N_{grid}}$ computation of E_{H} in Eqn. 4 avoiding the unfavorable scaling of the multi-center integrals by a direct computation in real-space using $\varphi_{\mu}(\mathbf{r})$. The construction of the XC potential in the GPW approach is identical to the plane-wave implementation in section 2.1. Finally, the KS matrix is calculated directly in real-space using an efficient algorithm that takes advantage of a compact representation of $\varphi_{\mu}(\mathbf{r})$ and scales as $O(\mathrm{N_{states}})$ [45]. The compact representation of $\varphi_{\mu}(\mathbf{r})$, previously alluded to, also ensures that the KS matrix is sparse, and its diagonalization and subsequent application to $\varphi_{\mu}(\mathbf{r})$ can also be performed efficiently[46]. Thus, it is clear that the GPW method has the potential to perform calculations of large systems with remarkable efficiency. Having said that, there are some drawbacks to the method that should be briefly mentioned. First, the quality of a plane-wave calculation is controlled by a single variable, namely the reciprocal-space cut-off for the plane-wave expansion, $\mathbf{G}_{\mathrm{cut}}$. The GPW calculation will depend on the quality of the basis (thus significant knowledge of traditional electronic structure calculations such as inclusion of split valence scheme or polarization function[47]) as well as the reciprocal-space cut-off for the plane-wave expansion of the density. Unfortunately, with the presence of atom-centered basis functions, we introduce the BSSE. The BSSE arises because of the dependence of the basis set on atomic positions. This gives arise to a non-uniform spatial variational flexibility that artificially lowers the energy. The effect of the BSSE on the condensed phase environment has yet to be fully understood. The performance of the methods outlined in this section applied to systems relevant to this review will be discussed in section 5.

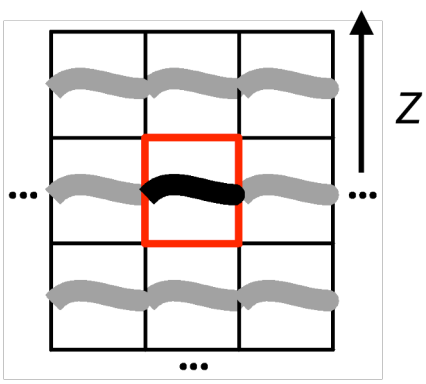

Figure 2: The central un-replicated supercell is depicted in red and contains the original interface with its two free surfaces, in black. Periodically replicated images of the interface are denoted in grey.

2.3 Boundary conditions

One approach to simulating an interfacial system is to set up the system in slab geometry where the interface occupies the central portion of the supercell (see Figure 2). If one is dealing only with short range interaction potentials (*i.e.* Lennard-Jones potential) an elongation cell in the *z*-direction (perpendicular to the interface) such that the two free surfaces are outside the potential energy cut-off, is sufficient to achieve a true 2D slab geometry. When one decides to employ long-range potentials, which are common place in the simulation of aqueous systems (*i.e.* electrostatic potentials), one has to approach the situation with caution. It's clear from Figure 2, in the presence of electrostatics, if the two free interfaces are not sufficiently far apart they could interact. Practically speaking, for MD simulations utilizing classical empirical potentials with point charges, the computational efficiency of the smooth particle-mesh ewald sum is efficient enough that one can include enough vacuum in the *z*- direction to again effectively reduce the problem to a 2D slab geometry[48] (see Figure 3). For first-principles approaches, in particular within the plane-wave formulation of KS-DFT, simply adding 100Å of vacuum will render any problem computationally intractable. Because the plane-wave basis set gives an equal representation over the whole supercell regardless of the position of the nuclei (see section 2.1), the basis will fill the entire supercell increasing the number of plane-waves as the volume, V (*i.e.* O(V)). In the hybrid approach discussed in section 2.2, basis functions are centered on atoms and thus there is no additional cost due to the increasing the number of basis functions. However, in formulation outlined in section 2.2, one still computes the electronic density, $n^{PW}(\boldsymbol{r})$ in the plane-wave basis which will scale linearly with the volume, O(V). Whereas, in the plane-wave approach, the density is computed via N_{states} FFTs all which scale as O(V),

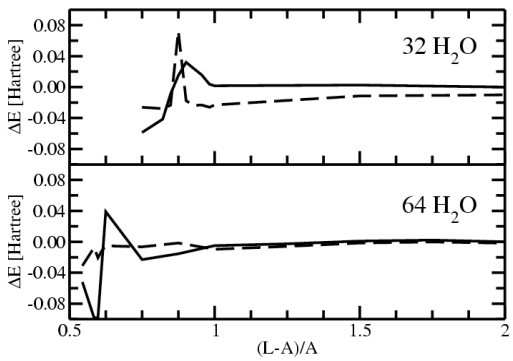

Figure 3 Energy convergence as a function of the supercell size in *z* direction (*L*) Solid line represent the use of 2D boundary condition while dash line represent the use of 3D boundary condition. using a constant interfacial width(*A*). Interfacial width (*A*) for 32 H_2O and 64 H_2O are 9.86 Å and 19.72 Å.

giving an overall $O(N_{states}V)$ scaling to compute the density in the presence of vacuum. The take home message of this analysis is that in periodic formulations of KS-DFT using the hybrid method presented in section 2.2 or plane-wave approach, the cost of vacuum is $O(V)$ and $O(N_{states}V)$, respectively. Thus, to save on computational cost and, more importantly, to perform a sound simulation representing the slab geometry (see Figure 1), a 2D-implementation of the long-range interactions should be used.

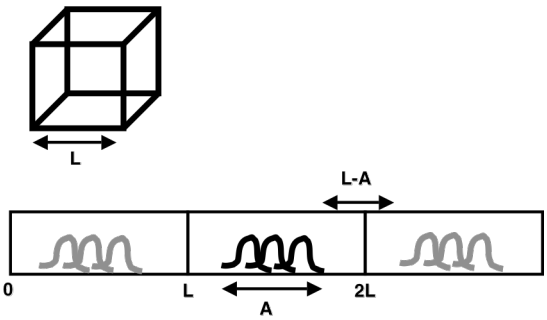

Figure 4: The isolated cluster (cube) and its periodic replication. The central charge density is represented in black and the first two images to left and right are represented in grey.

Fortunately, there are many decoupling schemes that can be used, and all of them have roughly the same computational expense[49-51]. All, are in principle exact, and only differ in the details of the implementation. For this review we will focus on the analytical de-coupling schemes[24,49-51], which we believe yields the most insight into the problem of decoupling periodic images. Any formulation of computing the long-range interactions yields the following integral

$$E_{\mathrm{LR}} = \frac{1}{2}\int_V d\mathbf{r}\int_{\text{all space}} d\mathbf{r}'\; n(\mathbf{r})n(\mathbf{r}')\Phi(\mathbf{r}-\mathbf{r}'),$$

Eqn. 13

where $\Phi(\mathbf{r}-\mathbf{r}')$ denotes the potential energy function[50].

To illustrate the method we will first compute the fully decoupled potential for the so-called cluster boundary conditions, *i.e.* isolated system. For the case of an isolated cluster, the potential can be written,

$$\Phi(\mathbf{r}) = \begin{cases} 1/r, & r > r_c \\ 0, & r \geq r_c \end{cases}.$$

Eqn. 14

Here, r_c is given by $A < r_c < L\text{-}A$ as depicted in Figure 4. Using the common form of the reciprocal space

density,

$$n(\mathbf{r}) = \frac{1}{V}\sum_{\mathbf{G}} \exp(i\mathbf{G}\cdot\mathbf{r}) n(\mathbf{G})$$

Eqn. 15

we obtain a final expression for the long range (LR) energy functional

$$E_{\mathrm{LR}} = \frac{1}{2V^2}\int_V d\mathbf{r}\sum_{\mathbf{G}} \exp(i\mathbf{G}\cdot\mathbf{r})\int d\mathbf{r}'\sum_{\mathbf{G}'} \exp(i\mathbf{G}'\cdot\mathbf{r}')\Phi(\mathbf{r}-\mathbf{r}')n(\mathbf{G})n(\mathbf{G}').$$

Eqn. 16

The screened potential for an isolated system (complete decoupling of all images), is given by

$$\Phi^{0\mathrm{D}}(\mathbf{G}) = \int_{r'<r_c} dr' \exp(i\mathbf{G}\cdot\mathbf{r})\frac{1}{r'} = \frac{4\pi}{G^2}\left[1-\cos\left(Gr_c\right)\right].$$

Eqn. 17

This is distinct from the fully periodic 3D potential which has the usual form of $4\pi/G^2$.

For the case of 2D we will derive an appropriate screening potential to be added to the full 3D potential, $4\pi/G^2$. To proceed, we subtract the region outside of the slab region defined from $z=-C/2$ to $C/2$ (see Figure 2). Thus, we are left with the following expression in analogy with Eqn. 17.

$$\Phi^{2\mathrm{D}}_{\mathrm{screen}}(\mathbf{G}) = -\int_{\mathrm{slab}} d\mathbf{r} \exp(i\mathbf{G}\cdot\mathbf{r})\frac{1}{\mathbf{r}}$$

Eqn. 18

We adopt cylindrical coordinates, z, r, and θ where the reciprocal space vector takes the following form, $\boldsymbol{G}=(g\cos\theta, g\sin\theta, g_z)$. Thus, we have

$$
\begin{aligned}
\Phi^{2D}_{\text{screen}}(\mathbf{G}) &= -2\int_{C/2}^{\infty} dz \exp(ig_z z)\int_0^{2\pi} d\theta \int_0^{\infty} r dr \exp(igr\cos\theta)\frac{1}{\sqrt{z^2+r^2}} \\
&= -2\int_{C/2}^{\infty} dz \cos(g_z z)\int_0^{\infty} 2\pi r dr J_0(gr)\frac{1}{\sqrt{z^2+r^2}} \\
&= -4\pi\int_{C/2}^{\infty} dz \cos(g_z z)\frac{1}{g}\exp(-gz) \\
&= \frac{-4\pi}{G^2}\exp(-gC/2)\left[\cos(g_z C/2) - \frac{g_z}{g}\sin(g_z C/2)\right]
\end{aligned}
$$

Eqn. 19

Using the definition of the reciprocal vector in an orthorhombic box, namely $g_z = n_z(2\pi/C)$, we obtain a final expression of the 2D screening function[24,51]:

$$
\Phi^{2D}_{\text{screen}}(\mathbf{G}) = \frac{-4\pi}{G^2}(-1)^{n_z}\exp(-gC/2).
$$

Eqn. 20

Similar formulations of 2D boundary conditions have been utilized with success[52,53] and use of Eqn. 20 to study aqueous liquid-vapor interfaces will be discussed in detail in section 5.

3 Spectroscopic observables

Though the cost of using a first-principles interaction potential to study heterogeneous systems can be prohibitive, there is direct access to the spectroscopic observables and reactivity. In particular, the use of first-principles interaction potentials in periodic geometry can make direct contact with infrared, Raman, and x-ray absorption experiments. In section 3.1 we will discuss the computation of infrared spectra from first-principles MD in the condensed phase, followed by the computation of Raman spectra using linear response theory in section 3.2. Last, we will give an overview of recent developments in the computation of x-ray absorption (XAS) in aqueous systems in section 3.3.

Since we are discussing interfacial systems, an experimental technique often used in the that takes advantage of the inherent anisotropy produced by the interface is the sum frequency generation (SFG)

technique. The formal theoretical framework for the computation of SFG spectra is well developed.[54-56] However at present, the computational cost to compute SFG spectra within a first-principles MD simulation is not computationally feasible.

3.1 Infrared

Infrared (IR) spectroscopy is generally one of the most readily available spectroscopic tools. In the case of water, IR absorption reveals the underlying dynamics of water such as its vibrational mode, bending mode, librational modes, and other intermolecular interactions. As a result, the ability to theoretically compute the IR absorption of any simulated systems is ideal in helping experimentalist interpret data with atomistic detail.

There is extensive literature on the computation of IR absorption using empirical force fields. Unfortunately, most of these methods suffer from the uncertainly in the calculation of electronic dipole which is necessary to compute the intensity of the IR absorption correctly. Unlike MD simulations utilizing classical empirical potentials, first-principles simulations should not suffer from this problem because the electric dipole moment is, in principle, available in any electronic structure calculation. The IR absorption coefficient, $\alpha(\omega)$, can be calculated as

$$\alpha(\omega) = \frac{4\pi\omega \tanh(\beta\hbar\omega/2)}{3\hbar n(\omega) c V} \times \int_{-\infty}^{\infty} dt e^{-i\omega t} \langle \mathbf{M}(t) \cdot \mathbf{M}(0) \rangle$$

Eqn. 21

where the use of classical nuclei is taken into account by the factor of $\tanh(\beta\hbar\omega/2)$, and $n(\omega)$ is the refractive index, and $\mathbf{M}$ is the dipole moment.[57] The autocorrelation function for the total electronic contribution (ionic and electronic), $\langle \mathbf{M}(t) \cdot \mathbf{M}(0) \rangle$ can be computed directly from a first-principles simulation. One of the main problems with the computation of the electronic dipole moment is the inability to precisely define the position operator in a periodic system. A clever solution was found to this problem by utilizing the so-called Berry's phase approach and computing the object[57-59],

$$S_{mn} = \langle \psi_m | \exp(-G_\alpha \cdot r) | \psi_n \rangle$$
$$\varphi(G_\alpha) = \mathrm{Im} \ln \det \mathbf{S}$$
,

Eqn. 22

for reciprocal lattice vector G_α. In the Berry's phase picture, the electronic dipole moment is computed as

$$M_\alpha^{\mathrm{el}} = \frac{2|e|}{|G_\alpha|} \varphi(G_\alpha).$$

Eqn. 23

Further details of this procedure can be found in Refs [57,58].

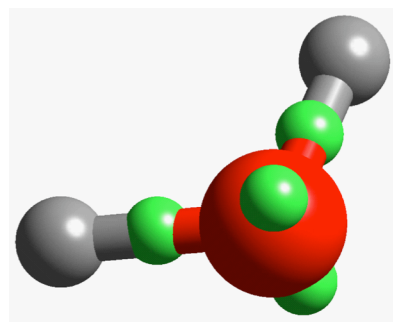

Figure 5 WF centroids (green spheres) of an isolated water molecule. Note that the two bond centered centroids and lone-pair centroids form a tetrahedron and carry charge $2e$.

Although IR absorption is highly useful in elucidating dynamical behavior for both intramolecular and intermolecular interactions, the problem in using Eqn. 23 to compute IR adsorption for the study of an interfacial systems is that Eqn. 23 is based on the total dipole moment, and thus surface effects may be washed out. Fortunately, first-principles simulation also affords one a local picture of the system dipole moment. A good approximation to the IR spectra is based on the computation of the charge centers of the molecule. Assuming that these charge centers carry the full electronic charge, and a known nuclear charge, we can compute the dipole moment for each individual molecule, and use Eqn. 21 with $\mathbf{M} = \sum_i \mathbf{M}_i^{\mathrm{mol}}$, where $\mathbf{M}_i^{\mathrm{mol}}$ is the dipole moment of the ith molecule. In practice, this partitioning of the charges is done through the maximally localized Wannier functions (WFs). The determination of the WFs is based on the Berry's phase approach outlined above. The WFs procedure can be boiled down to finding a unitary transformation that minimizes the spread, Ω_i of each orbital[60,61]

$$\Omega_i = \langle \mathbf{r}_i^2 \rangle - \langle \mathbf{r}_i \rangle^2.$$

Eqn. 24

The position expectation value of the position of the WF is given by

$$r_\alpha = \frac{2\pi}{L}\tilde{S}_{mm}$$
$$\tilde{S}_{mn} = \langle \psi_m U | \exp(-G_\alpha \cdot r) | U\psi_n \rangle$$

Eqn. 25

where the U is the unitary transformation that minimizes the total spread, $\sum_i \Omega_i$ (we also assume that we are in a square simulation cell such that G_α=2π/L). The WF centers and functions are shown for a single water molecule in Figure 5.

3.2 Raman

Unfortunately, IR spectroscopy cannot always capture dynamical modes for all molecular systems. In particular IR spectroscopy can only probe active modes where there is a change in molecular dipole. For Raman spectroscopy, the allowed transitions are those where the polarizability of a molecule changes. Thus, making IR and Raman spectroscopy complementary techniques. From first-principles MD simulation, it is possible to directly compute the Raman spectra within the Berry phase scheme by computing the Fourier transform of the autocorrelation for the dynamic polarization tensor, $\overleftrightarrow{\alpha}(t)$, within the variational density functional perturbation theory. [62] The polarizability tensor can be computed numerically as

$$\alpha_{\mu\nu}(t) = \frac{\partial^2 E}{\partial E_\mu \partial E_\nu}$$

Eqn. 26

throughout the simulation.[63] Quantum effects can also be incorporated if classical nuclei are used by multiplying by the factor $\left[1-\exp(-\hbar\omega/k_B T)/2\right]$.[64] But more specifically, the polarizability tensor can be separated into isotropic and anisotropic contributions, where the isotropic contribution to the Raman spectra is

$$I_{ISO}(\omega) = \frac{N}{2\pi}\int_{-\infty}^{\infty} dt e^{-i\omega t}\left\langle \overleftrightarrow{\alpha}(0)\cdot\overleftrightarrow{\alpha}(t)\right\rangle$$

Eqn. 27

and the anisotropic piece is

$$I_{ANISO}(\omega) = \frac{N}{2\pi}\int_{-\infty}^{\infty} dt e^{-i\omega t}\,\tfrac{1}{10}\left\langle \mathrm{Tr}\left[\overleftrightarrow{\beta}(0)\cdot\overleftrightarrow{\beta}(t)\right]\right\rangle$$

Eqn. 28

and the total intensity is $I(\omega) = I_{ISO}(\omega) + \tfrac{4}{3} I_{ANISO}(\omega)$.[65] Like the simulated IR spectra, the calculation of Raman spectroscopy from first principles simulation is a powerful tool that can compliment experiments giving a particle-based picture to the spectroscopic signature.

3.3 X-ray

Altthough x-ray absorption spectra (XAS) is widely used in technique in surface science, its utility in elucidating new insights into the structure of soft materials (including liquid-vapor and solid-vapor interfaces) is at its infancy. In particular, recent XAS experiments on water have has challenged the conventional view of the structure of both bulk[66,67] and interfacial water.[68,69] Therefore, the ability to compute XAS from first-principles MD simulation will be of unique interest to experimentalist in helping to decipher spectra from XAS.

Unlike IR and Raman spectroscopy discussed in sections 3.1and 3.2 that can be computed utilizing classical models for the dipole and polarizability, XAS is relies on some level of quantum theory to make contact with experimental spectra. The oscillator strengths in XAS can be written as

$$I_{if} = \tfrac{2}{3}\Delta E_{if}\left|\left\langle \psi_i \middle| \mathbf{r} \middle| \psi_f \right\rangle\right|^2$$

Eqn. 29

Here, the subscripts *i* and *f* denote initial and final states, respectively. The quantum chemical analysis that is necessary for the computation of the XAS spectra for aqueous systems has been employed in conjunction with configurations generated from MD utilizing classical empirical interaction potentials[70].

These calculations indicate that there is a large sensitivity of the computed XAS spectra to the distinct hydrogen-bonding configurations present in liquid water[70]. However, this type of analysis is vulnerable to the differences in the classical force field from the quantum chemical model. Thus, a fully self-consistent first-principles treatment is preferable, if not imperative. It has recently been shown[71] that one can compute the XAS spectra of liquid water within the transition potential approach of DFT[72,73]. The XAS spectrum is from the analysis of a single wave function where the core level has half an electron removed ($1s^{1.5}2s^2 2p^4$). It is known that the use of a half-occupied core hole takes care of relaxation effects up to second order. These researchers[71] have implemented this scheme in **CPMD** within the PP approximation. Although similar calculations have been performed within the CP-MD framework, differences in implementation have been focused around the reconstruction of the all electron wavefunction from the pseudo wavefunction of the final state for use in the transition probability[74,75] The dipole selection rule for the specific case of aqueous systems, implies that transitions from a 1*s* core level will be sensitive to the local *p*-character of the valence wavefunction[71]. Given this, the authors of Ref.[71] determined that that for first-row elements (such as oxygen) that the pseudo *p*-character in the valence wavefunction is very close to the all-electron counter part. It was found that the difference in oscillator strengths for a variety of clusters using pseudo and all-electron valence wavefunctions is negligible[71].

4 Solid-vapor interfaces

As was alluded to in section 1, large-scale first-principles modeling is at its infancy with regards to finding solutions to the myriad of fundamental questions in atmospheric science. However, given that first-principles calculations of heterogeneous systems require sizable computational resources, it has not stopped researchers from making significant progress towards understanding important atmospheric processes[3,6,76-85]. One instance where first-principles calculations have made significant progress toward understanding problems in atmospheric science is in the field of ozone depletion. In particular, the role

of the solid-vapor interfaces in the depletion of Artic and Antarctic ozone is of particular interest to the atmospheric community. The current conventional wisdom is that chlorinated compounds such as HCl and $ClONO_2$ are sequestered in polar stratospheric clouds (PSCs)[86-90]. There are two predominant PSCs: the first (called type I) is thought to comprise of nitric acid trihydrate (NAT). The second (type II) is though to be ordinary ice[86-90]. Moreover, it has been experimentally verified that ice can act as a catalyst to reduce the barrier of reactivity to otherwise unreactive chlorinated gas phase species (*e.g* HCl, HOCl, and $ClONO_2$)[5]. Thus, it is heterogeneous chemistry that will give rise to the production of the activated Cl_2(g) via the proposed set of reactions.

$$ClONO_2(g) + H_2O(s) \xrightarrow{PSC} HOCl(g,ads) + HNO_3(ads)$$

Eqn. 30

$$HOCl\ (ads) + HCl(ads) \xrightarrow{PSC} Cl_2(g) + H_2O$$

Eqn. 31

$$ClONO_2(g) + HCl(ads) \xrightarrow{PSC} Cl_2(g) + HNO_3(s)$$

Eqn. 32

Eqn. 30 and Eqn. 31 comprise a two step mechanism, whereas Eqn. 32 is a single step to form the active Cl_2(g) product[91,92]. Upon examination of the aforementioned mechanisms, it becomes clear that the role of the interaction of HCl with the PSC provides a common denominator. Thus, there have been numerous experimental and theoretical studies designed to understand the uptake of HCl and its concomitant chemistry[76,93-116]. Measurements have characterized the uptake of HCl on well characterized ice films (prototypical type II PSCs) yielding results ranging from $2(10^{13})$-$4(10^{14})$ molecules/cm^2 under conditions approaching a PSC[5,117,118]. A variety of experiments indicate that ionic hydrates of HCl on ice films form at monolayer coverage (*.e.g.* $1(10^{15})$ molecules/cm^2)[101,102,105,106,113,115,116,119]. Conversely, experiments at sub-monolayer coverage suggest that molecular HCl absorbed on the surface, however experiments are difficult to conduct and interpret within the conditions approaching a PSC, thus motivating the use of molecular simulation[103,104,106,120-122].

Attempts to understand and verify the above mechanisms have been addressed with large simulations based on pure classical empirical interaction potentials, reactive empirical interaction potentials, and first-principles interaction potentials in conjunction with smaller cluster models[84,93-100,108,109,112,123-129]. However, there is an emerging class of studies using first-principles interaction potentials of the more realistic semi-infinite surface based on methods outlined in sections 2.1-2.2[3,6,76-82].

The idea of using a semi-infinite slab geometry to model the reactive interfaces is not done solely for the sake of vanity. It has long been known that surfaces of many solids can be disordered below the freezing point of the bulk liquid[130]. For example, there is speculation that the surfaces of type II PSCs may be disordered (quasi-liquid) and can lead to the enhancement of the uptake of HCl. Naturally, this can only be modeled with a semi-infinite geometry depicted in Figure 1[123,124,127,128,131-137].. The propensity, if not the existence, of the so-called quasi-liquid layer to aid in sequestering chlorinated compounds as well as NO_x byproducts is not understood[6,11,80,82]. Although experimentalists have produced a picture where surface ice is distinct from bulk, the temperature of this surface disordering effect is difficult to pin down due its sensitivity to thermodynamic conditions (*e.g.* pressure), impurities, and to the dependence on the different spectroscopic probes[123,124,127,128,131-137]. Thus, the use of first-principles simulation techniques may provide new insights into this difficult, but important problem. Surprisingly, there have been more first-principles studies of type II PSC interacting with a chlorinated species than the corresponding clean type II PSC.

The role of type I PSCs in chorine activation is currently less understood than that of type II. It is known from experiments that the efficiency of Cl_2(gas) production on NAT is strongly correlated with humidity, and at a greatly reduced rate than the corresponding rate on type II PSCs[138]. Thus for a specific set of conditions there can be "H_2O-rich" or "HNO_3-rich" NAT yielding very different catalytic behavior[81,138]. Experiments on the uptake of HCl on NAT have also been performed on surfaces resembling something in between "H_2O-rich" and "HNO_3-rich" NAT yielding coverage similar to those measured on well-prepared ice surfaces[5,118]. However, experiments performed on the uptake of HCl on

"HNO_3-rich" NAT indicate coverage about an order of magnitude less than those corresponding to the well prepared ice surfaces resembling type II PSCs[138].

Thus, the goal of large-scale first-principles calculations reviewed here will be aimed at addressing the following issues regarding the structure and reactivity of PSCs:

i. The existence of the quasi-liquid layer (type II)

ii. The role of the quasi-liquid layer to yield the proposed catalytic activity (type II)

iii. Predict the observed uptake and concomitant reactions of HCl on PSCs (type I and II)

iv. Examine possible heterogeneous reaction mechanisms leading to Cl_2(g) (type I and II)

4.1 Ice

First-principles research regarding the nature of ice-vapor interfaces and the concomitant chemistry that can occur has recently been examined. The first set of simulations that will be reviewed are performed with both static and dynamic plane-wave calculations utilizing the **CPMD** code outlined in section 2.1. In these studies, a supercell of hexagonal basal (0001) face of ice I*h,* which is thought to be the predominant surface under polar stratospheric conditions, is considered[91,92]. From Figure 6, the 32 water molecule supercell is made up of four bilayers. Again, as pointed out in section 2.3, there are two free surfaces which must be kept from interacting by using either the appropriate 2D boundary conditions described in section 2.3, or adequate amount of vacuum. Of course, vacuum comes at a price for the plane-wave approach (see section 2.3) and the delicate balance of amount of vacuum and computational efficiency must be considered. The aforementioned plane-wave calculations utilize vacuum ranging from 6 to 8 Å depending on the type of calculation being performed. The use of the Nose-Hoover thermostat was utilized for temperature control over the duration of the production runs[139,140].

To deduce the presence of a quasi-liquid layer, four first-principles simulations were performed over a temperature range of 190K-310K to investigate the effects of temperature on the formation of the quasi-liquid layer[80]. All four simulations were run for a duration of 1 ps with the fourth bilayer constrained not to move in order to better approximate a semi-infinite slab; thus effectively simulating one free interface[80]. One of the key findings was that the (0001) surface of ice is significantly disordered at 190K. This is in contrast to the melting point for the 32 atom supercell of the ice surface which was estimated to be at 220K, which is below experiment[80].

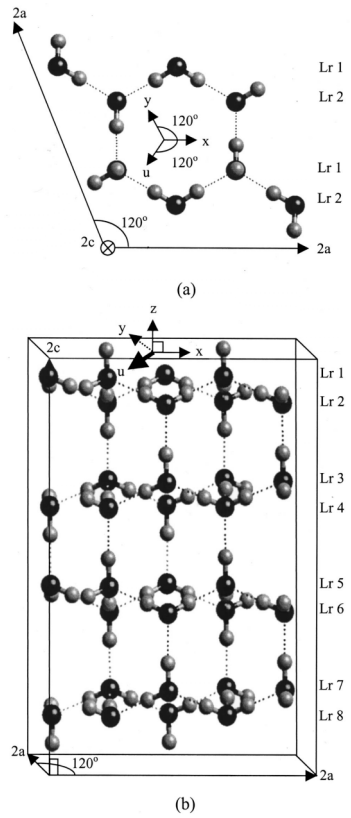

Figure 6: Supercell of hexagonal ice reproduced from Ref. [6]. Top panel represents the basal (0001) plane. Bottom panel is one of the six prism faces where the four bilayers are visible (*i.e.* Bilayer 1 is made up of layers 1 and 2). Dotted lines represent hydrogen bonds between oxygen (black) and hydrogen (grey).

Indicators of the onset of surface disordering yielding a quasi-liquid layer are borne out when examining translational and rotational order parameters for the individual bilayers (see Figure 6). The order parameters used by Mantz *et. al* were identical to those proposed in a similar study utilizing classical empirical potentials[141]. The findings regarding the rotational and translational order parameters using first-principles interaction potentials were in good agreement with the classical empirical potentials given the caveat of trajectory length[141]. Translational disorder was also quantified in the *z* direction by computing average displacements from the fourth, fixed bilayer[80]. The results of this calculation corroborated experimental observations that layer 1 of bilayer 1 becomes disordered at 190K whereas bilayers 2-3 remain ordered. A continuous transition to complete melting of the supercell was observed as the temperature is increased. Other indicators of the disordering are gleaned through examination of the radial distribution function (RDF) and mean square displacement (MSD) performed layer-by-layer[80]. Using a reasonable guess for the normalization of the RDF for the layers, convincing evidence of a disordered

first bilayer is obtained at 190K with a first-peak height approaching that of a simulated bulk liquid of 32 water molecules[80]. The MSD at 230K also seem to agree very well with a simulated bulk liquid indicating a melt. However, given the extremely short simulation time, these results are most likely fortuitous. Having said that, the relative difference between the MSD of the different bilayers at 230K and 190K clearly point to the picture of a surface disordering at temperatures less than the bulk melting point. Last, a final simulation was performed to assess the effect of allowing bilayer four to remain free[80]. Properties that were affected were the heat capacity (presumably due to the additional degrees of freedom). The effects of fixing the 4th bilayer on the translation and rotational order parameter, as well as displacement in the *z* direction were inconclusive. In other words, the two free surfaces (bilayer 1 and 4) did not behave identically[80]. However, this is most likely due to the extremely short simulation times that are required to equilibrate two free surfaces. This will be discussed in more detail in section 5.

Given the usual caveats of system size, choice of density functional, and trajectory length, there is certainly strong evidence put forth for the existence of a quasi-liquid layer using KS-DFT. The next step is to examine the role of microsolvation of chlorinated species (HCl, HOCl, and $ClONO_2$) leading to the proposed catalytic activity of the ice surface and the formation of activated Cl_2(g) via Eqn. 30 and Eqn. 31. For studies of mechanisms leading to the activated Cl_2(g), both dynamic and static studies utilizing plane-wave and localized orbital schemes have been employed.

Calculations were performed on supercells of hexagonal basal (0001) face of ice I*h* interacting with HCl[76,77]. Static studies utilizing localized orbitals within a periodic formulation of HF[29-31] were performed on a 1x2 supercell of ice (as opposed to the 2x2 supercell of Mantz *et al.*[80]) and focused on understanding the relative stabilities of molecular versus ionic HCl on the surface of ice[77]. After BSSE and correlation effects were taken into account, their findings indicated that it was energetically favorable to have molecular HCl inserted into an inclusion where a single surface water was displaced[77]. Furthermore, periodic substitution of HCl was favored more than a single HCl molecule leading to the

conclusion that cooperative effects are indeed important[77]. Although the energetics of substituted HCl molecule was not as favorable as neat ice surface (differing by 10-15 kcal/mol) it was found that the substitution of Cl^- and H^+ into the surface of ice was nearly isoenergetic (differing by 2-4 kcal/mol)[77]. These static calculations indicate that the dissociation of HCl to form ionic hydrates is most likely spontaneous and can lead to surface sites with exposed chloride and can give rise to novel heterogeneous chemistry in line with experimental observations[113,116]. However, after chloride was inserted into subsurface layers, the resulting geometries were unstable leading to the conclusion that chloride will most likely remain on the surface at odds with the conclusions using empirical models[91,92].

Static plane-wave calculations utilizing both HF[76] and KS-DFT[82] were also performed to better understand the interaction of ice with HCl. In the KS-DFT study, particular attention was focused on the role of dangling bonds in promoting the dissociation of HCl[82]. Both 16[76,82] and 32[82] water molecules were used (2x1 and 2x2 supercell). In the KS-DFT study, surfaces with different number of free (dangling) OH bonds were generated by considering all possible configurations where the hydrogen atoms satisfied the Bernal-Fowler ice rules[82]. Geometry optimizations were performed with the HCl molecule above the surface plane for five different slab conditions in the KS-DFT study (see Figure 7)[82]. Under the same conditions that were utilized in the HF study (*i.e.* 16 molecule supercell, one HCl adsorbate, and two dangling OH bonds) results agreed to within 3 kJ/mol indicating that different levels of theory give consistent results[82].

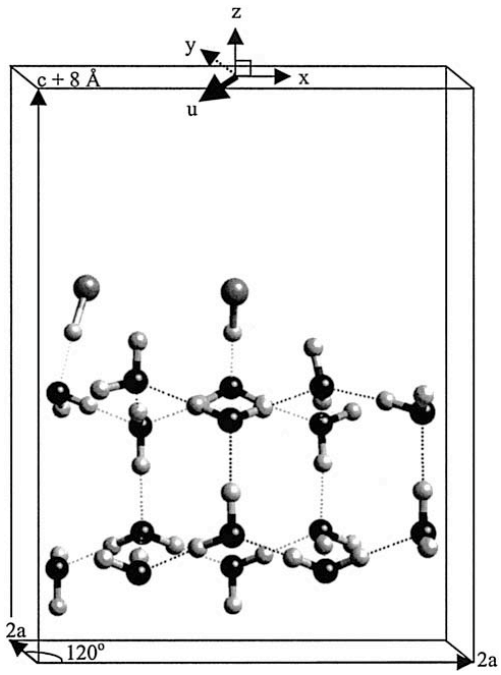

Figure 7: Side view of the one 6 prism faces perpendicular to the (0001) basal plane of ice depicting the initial configurations of two HCl molecules reproduced from Ref.[6]. The supercell and vacuum region are superimposed. Color coding is the same as in Figure 6 and Cl is represented by large grey spheres.

The results from the KS-DFT study suggest that the HCl adsorbed more favorably to sites where more free OH bonds are present in line with some experimental findings[82,103,104].

This could clearly be an indication of the microsolvation effects of a cluster of free OH groups stabilizing on the $Cl^{\delta-}$. Binding energies were also examined as a function of coverage[82]. For low coverage (1.4(10^{14}) molecules/cm^2) the binding energies were slightly higher than for coverage sapproaching that of a monolayer (2.8(10^{14}) molecules/cm^2). Although the binding energies for low coverage were in agreement with cluster models resembling the surface geometry[76,77,108,142], no dissociation was observed, although there was a lengthening of the H-Cl bond of 7%. Last, the results of the KS-DFT study pointed to a picture where HCl binds more favorably to sites containing more free OH bonds, though it is not clear that surfaces with a high density of free OH bonds are representative of type II PSCs[82,143].

The dynamic effects of the adsorption of HCl on the hexagonal basal (0001) face of ice I*h* was also examined within a plane-wave formulation of KS-DFT[6]. Starting from an optimized configuration of an HCl above the (0001) face (see Figure 7), MD trajectories were performed at three different HCl adsorbing sites: (1) to deduce the propensity for dissociation as a function of surface population of dangling OH bonds, (2) examine the role of HCl on the disordering of the ice surface. From this study it was found that spontaneous dissociation of HCl into H^+ and Cl^- is observed when an HCl molecule is interacting with a surface site containing two dangling OH bonds[6]. When geometry optimization were performed at intermediate points of the trajectory it was found that there was a 20 kJ/mol additional stabilization over the molecularly absorbed HCl[76,82 84]. Conversely, when HCl is absorbed over a site with only one free OH bond, or placed further away from dangling OH bonds, no HCl dissociation was observed[6]. To understand these interactions, two simulations of a H_3O^+ and Cl^- placed on previously optimized ice slab were performed. One simulation yielded the stable formation of a contact ion pair and the other, molecular HCl[6]. The binding energies of the contact ion pair and the molecular HCl compared well to optimized structure of the HCl-ice system. This lead the researchers to conclude that dissociation of HCl is thermodynamically favorable under the appropriate conditions[6].

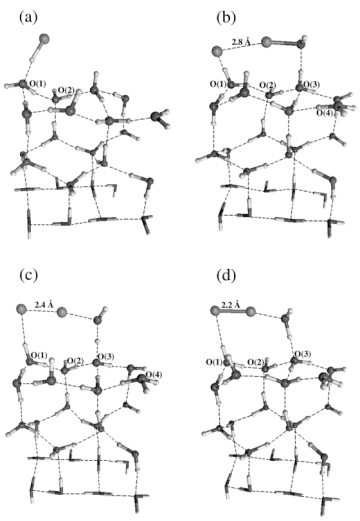

Figure 8: Details of the four step reaction mechanism proposed in Ref. [5]. Color coding is the same as in Figure 7.

Another question that can be addressed is the role of HCl on the formation of the quasi-liquid layer. Recall, that Gertner and Hynes, employing an empirical interaction potential, conjectured that dissociation of HCl was spontaneous and independent of the presence of a quasi-liquid layer[91,92] which corroborate the results of the static localized orbital study[77]. Using the data generated with the dynamical study of HCl on ice, researchers examined the first peak of the oxygen-oxygen RDF in order to gauge the effects of surface disordering in the presence of associated and dissociated HCl. For the case of dissociated HCl at 150K, the oxygen-oxygen RDF for bilayers 1 and 2 is similar to those obtained for the neat ice surface at 230K[6,81]. In the presence of associated HCl, the oxygen-oxygen RDF is sharper than that of the theoretically predicted surface disordering temperature that the clean ice surface at 190K. Thus, the results suggest that for high surface coverage of HCl in the presence of two dangling OH bonds, the disordering temperature is significantly depressed and extends into the second bilayer. For the hypothetical case of a larger system with no quasi-liquid layer present, that disordering may be a local phenomenon and thus a conjecture is made that one could be in agreement with the work of Gertner and Hynes layer[91,92].

Finally, two detailed first-principles studies of Eqn. 30 were performed with seemingly very different conclusions[3,79]. The first study was performed with a plane-wave formation of KS-DFT using a 2x1 supercell where an additional layer in the *z* direction was added yielding a total of 24 water molecules[79]. Furthermore, it made use of the so-called ultra-soft pseudo potentials allowing for a significantly reduced basis set cut-off and thus dramatically reducing the computational expense[35,144,145]. It should be noted the structural and dynamical properties regarding liquid water using the ultrasoft PPs in conjunction with the PBE functional are still not understood[25,26,146-148]. Nevertheless, the study shows that all reactions take place on the perfect hexagonal basal (0001) face of I*h* ice while neglecting any

surface disordering that may be present. Initial geometries of the HCl adsorbate used by these researchers were similar to those in previous studies[6,76,82]. Next, by introducing the HOCl gas molecule it was found that the Cl-Cl distance was roughly 3 Å (see step (a) in Figure 8)[79]. Because of the computational efficiency of the plane-wave formulation, potential of mean force calculations were performed utilizing the Cl-Cl distance as the reaction coordinate[144,145]. Each step of the free energy calculation was performed over roughly 1.5-2.5ps of equilibration. The results of this study lead to a picture where the ice surface interacting with a physisorbed HCl become highly catalytic[79]. Results of this study present a picture where the interacting HOCl molecule aids in the dissociation of the HCl molecule[79]. This view is slightly different than the previously reviewed studies that indicate the HCl molecule can spontaneously dissociate on the ice surface[6,77]. The findings of the plane-wave study suggest that the HCl dissociates and the proton quickly migrates between 2-3 waters (see step (b) in Figure 8) leaving an isolated Cl^- to interact with a physisorbed HOCl molecule (see step (c) in Figure 8)[79]. The formation of Cl_2 (g) and water continues to proceed spontaneously (see step (d) in Figure 8). Liu *et. al.* attribute the enhanced catalytic activity to the mobile proton that facilitates the formation of water in the last step (see Figure 8)[79]. The researchers also find that if one increases Cl-Cl distance in step (b) of Figure 8 the formation of molecular HCl through reverse proton migration is again achieved[79].

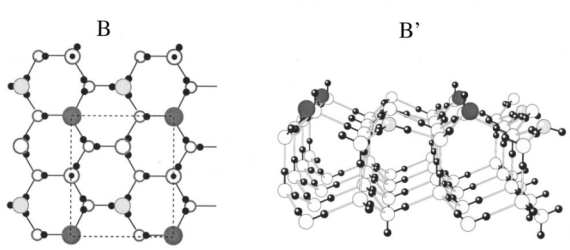

Figure 9: Top (B) and side views (B') of the chlorinated P_{hyCl} surface reproduced from Ref. [3]. Oxygen is small white circle, hydrogen is depicted by a small black filled circle, chloride is dark grey and the hydronium oxygen is light grey.

In a recent static first-principles study, a more involved reaction mechanism emerges when considering the reaction of Eqn. 31[3]. This study makes reference to the aforementioned dynamical study of the production of activated Cl_2(g)[79]. In particular, issues to the level of theory and the effects of the proton mobility which gives rise to the enhanced catalytic activity are questioned[3]. These

authors make use of a localized orbital formulation at the HF level of theory as was discussed previously in applications to ice surfaces and the adsorption of HCl on ice[76,77]. This careful study examined the energetics of the proposed structures using both a fully periodic system and molecular clusters[3]. The initial condition of this study does not assume the interaction of co-adsorbed species of HCl and HOCl, but rather the interaction of HOCl with an ice surface is already incorporated with Cl^- and H_3O^+ (see Figure 9) as described in earlier studies[77]. Thus, the sequence of reactions considered here given (in the notation of Ref. [3])

$$HCl + Ice \rightarrow P_{hyCl}$$

Eqn. 33

$$P_{hyCl} + HOCl \rightarrow Cl_2 + H_2O + Ice$$

Eqn. 34

The top bilayer and the side view of the HCl hydrated surface, P_{hyCl} is shown in Figure 9. More succinctly, these researchers considered the hypothetical reaction mechanism: (1) Activation of the surface through proton migration; (2) physiorption of HOCl with formation of H^+ - (OH) Cl – Cl^- complex; (3) concerted elongation of the O-Cl bond and proton migration towards the molecule; (4) formation of Cl_2(g) and H_2O[3]. The activatation of the P_{hyCl} species in step (1) occurs either via a two step proton migration, or a proton rearrangement to produce a surface H_3O^+ moiety with a dangling OH[3]. Once the surface has been activated, the energetics of physisorption of the HOCl is compared in two scenarios where either the H or the Cl is in contact with the surface[3]. Comparing the energetics of both these possibilities suggests that direct interaction of the H of the physisorbed species with the activated P_{hyCl} is always more favorable. Last, actual reaction energetics were examined that produce the activated Cl_2(gas) and water. Reaction mechanisms were followed through two forms of the activated P_{hyCl}, namely with proton movement (referred to P^1_{hyCl} in Ref [3]) and with proton rearrangement (referred to P^3_{hyCl} in Ref [3]). Both activated surfaces produced the same generic energy profile suggesting that reaction with these highly optimized ice surfaces is energetically costly barriers on the order of 30-50

kcal/mol[3].

If one examines all of the work that has been reviewed on the heterogeneous chemistry of ice-vapor interfaces, although the methods, configurations, and precise details of the studies differ, there seem to be strong consensus with the direction that this research. First, is agreement with all of the studies that HCl will not spontaneously dissociate on a perfectly ordered surface of ice. The degree that disordering is necessary, either through the presence of a quasi-liquid layer or defects, is still an open question although it should also be noted that recent XAS experiments point to a picture where the presence of dangling bonds may not play a major role in the sequestering and the subsequent reaction of HCl[119]. All of the first-principles studies suffer from small system sizes and sampling effects that are sure to have an affect on some of the conclusions that have been drawn. Thus, it is clear from the point of view of first-principles calculations (both static and dynamic) that there are still many unresolved questions pertaining to nature of heterogeneous chemistry at ice-vapor interfaces.

4.2 Nitric Acid Tri-hydrate

Recent first-principles studies have focused on bulk NAT[149] as well as the less atmospherically relevant nitric acid monohydrate (NAM)[83]. The appearance of first-principles calculations utilizing the KS-DFT method in conjunction with ultra-soft PPs on the NAM surface have also been performed presumably due to its smaller unit cell size (*i.e.* computationally more tractable)[85]. This study was carried out on 32 atom unit cell which is far short of the 32 molecule supercell that has been used for the type II studies reviewed in section 4.1. Three calculations were performed where an HCl, $ClONO_2$, and H_2O molecule was randomly placed over the (100) surface of NAM[85]. It was found that all three molecules adsorbed parallel to the surface ranging from 3.3-3.9 Å[85]. To test for catalytic activity, very short molecular dynamics simulations of 0.5 ps at 190K were performed where the three molecules were allowed to move from their geometry optimized configurations on the surface. There was no appreciable differences in adsorbate geometries found leading to the conclusion that NAM is not a

catalytic surface[85]. However, it is not clear that results gained from NAM surfaces will transfer over to NAT. Furthermore, large-scale studies of NAT surfaces are also hindered because there is no known classical empirical interaction potential to study bulk crystalline NAT and the status of HCl on NAT surfaces has not been experimentally determined[81]. Thus, it is absolutely necessary to us a first-principles interaction potential as a first step in the understanding of type I PSCs. To this end, a detailed static and dynamical study based on the plane-wave formulation of KS-DFT of the NAT-vapor interface and its interaction with HCl has been performed on a 112 atom 1x1x2 supercell[81].

In order to proceed, the determination of the thermodynamically favored low index faces needed to be selected. To this end, optimizations were carried out on six different low index facets, namely the (100), ($\underline{1}$00), (010), (0$\underline{1}$0), (001), and (00$\underline{1}$). The surface energy of the (001) face was found to be the lowest, suggesting that this face will be the most relevant to conduct detailed studies of the atmospherically relevant reactions[81]. By testing 54 different initial conditions of HCl over the (001) interface of NAT the relevant binding sites and geometries were determined[81]. It was found that 18 configurations produced a binding energy of at least 4 kJ/mol, but only one configuration with a binding energy of 27 kJ/mol[81] typical for adsorption energies on type II PSCs[6,76,82]. This could be seen as an indication that "HNO_3-rich" NAT does not sequester as much HCl as type II PSCs in line with experimental results[138]. The site with the greatest affinity for HCl involves and interaction with an NO_3^- ion and the possibility of interacting with at least one dangling OH bond of a nearby water[81]. Indeed, there are also two NO_3^- surface sites that would allow for the simultaneous interaction with two dangling OH bonds. When two trial configurations were optimized (HCl in the presence of one and two dangling OH bonds), it was found that even with the additional hydrogen bond formed with Cl^-, the two sites were nearly equal in energy[81] in contrast to studies on type II PSCs[6,82].

In order to determine the fate of the adsorbed HCl (*i.e.* whether it remains associated or dissociates), molecular dynamics calculation were performed from the optimized configurations with one and two dangling OH groups interacting with HCl. The dynamics of the HCl interacting with two dangling OH

groups produced a final configuration where the HCl was not interacting with either of the dangling OH bonds and was adsorbed perpendicular to the (001) interface[81]. Dynamical simulations from the geometry optimized HCl interacting with a single dangling OH bond produced dissociation and subsequent re-association of the HCl bond[81]. To further test the reliability of the dynamical results configurations were generated based on the geometry optimized interactions of HCl with one and two dangling OH bonds where HCl was dissociated. In all cases, after geometry optimizations were performed, it was found that the HCl remains associated at the (001) surface of NAT[81].

5 Liquid-vapor interfaces

Aqueous liquid-vapor interfaces can also play a role in determining the chemistry that can occur in the troposphere. The relevant heterogeneous chemistry that can occur in the troposphere has been recently reviewed by Finlayson-Pitts[150]. Although the understanding of the bulk phases of hydrogen-bonding fluids is far from complete, the scientific impetus to understand these systems in more complex environments is far reaching. Furthermore, elucidating heterogeneous chemistry in the presence of an inorganic electrolyte and resolving the discrepancy in the mass accommodation coefficients for gases at the water-air interface is of paramount importance in atmospheric science[12,151-153]. This has, in part, led to a recent surge of pioneering scientific investigations within the chemical physics community to develop new surface-sensitive experimental techniques over the past two decades[68,69,154-164]. Recent experimental findings have revealed unexpected molecular structure and electronic distribution present at liquid-vapor interfaces[68,69,154-164]. In turn, these sophisticated techniques lead to a new challenge of connecting the results of these state-of-the-art experiments to the desired information on the microscopic properties of these liquid-vapor interfaces. Thus, the aforementioned experimental findings have stimulated a new realm of computational investigations whose central objective is to elucidate the structural, dynamic, and electronic properties of these important interfacial systems.

The first detailed MD calculations of the aqueous liquid-vapor interface were performed fifteen to

twenty years ago employing empirical pair-wise additive potentials (Lennard-Jones and Coulomb interactions with fixed charges) as model for liquid water[165-167]. These studies were the first quantitative calculations providing both structural and thermodynamic information about this important system. Although these MD studies pre-date the advent of surface sensitive spectroscopies applied to the aqueous liquid-vapor interface, they have provided a template on which all subsequent MD studies were based which has been covered in section 3.

Starting ten years ago, pioneering spectroscopic investigations, using SFG technique, have provided an experimental picture of the detailed structure of the neat aqueous liquid-vapor interface[157,159-162]. These experiments pointed to structure at the interface being very distinct from the bulk. Two features in the spectra of these early experiments are noteworthy. First, a sharp peak at ~3700 cm^{-1} indicates the presence of dangling hydrogen bonds at the interface. The second is a pronounced shoulder attached to the prominent peak at ~3400 cm^{-1} present in bulk liquids that indicates the presence of a different hydrogen bonding arrangement at the surface. These SFG surface spectra of the neat liquid-vapor interface provided concrete data[157,159-162] that were amenable to a direct comparison with data obtained from MD simulations[168,169]. This MD study qualitatively elucidated the spectroscopic signals for both the existence of dangling OH bonds and the alternative hydrogen bonding arrangement at the surface.

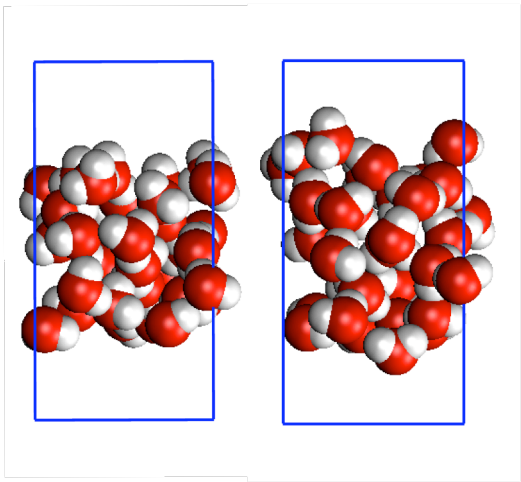

Figure 10: Side view (along *z*) of the initial (left) and final (right) configuration of a 32 water molecule aqueous liquid-vapor interface using full periodic boundary conditions with a supercell of *L*x*L*x2*L* (blue bounding box). After 5 ps of CP-MD, note the loss of a well defined interface. All CP-MD simulation parameters are identical to those in Ref. [2]. The supercell is superimposed in blue.

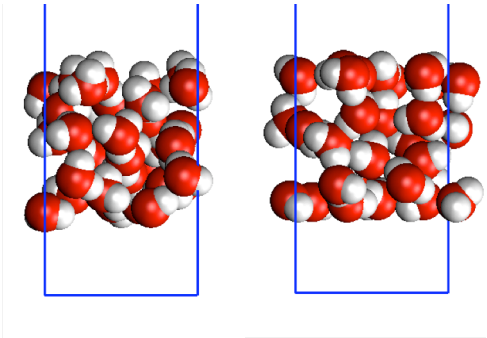

Figure 11: Side view (along *z*) of the initial (left) and final (right) configuration of a 32 water molecule aqueous liquid-vapor interface using 2D screening function with *L*x*L*x2*L* (blue bounding box). After 5 ps of CP-MD, note the presence of a well defined interface. All CP-MD simulation parameters are identical to those in Ref. [2]. The supercell is superimposed in blue.

Although it appears that classical empirical interaction potentials for water parameterized to reproduce bulk structural properties seem to perform well in the vicinity of the liquid-vapor interface. Despite that the structural properties are adequately reproduced for water, the thermodynamic properties, such as surface tension and phase equilibria, indicate a deficiency in fixed-charge empirical models. Thus, a substantial amount of effort directed at developing water models that incorporate the polarization present at the aqueous liquid-vapor interface[4,8,10]. Moreover, additional experimental investigations on neat interfacial systems have led to further characterization of liquid-vapor interfaces and highlight the need for more accurate models[68,69,154,156]. As alluded to in section 3.3 XAS investigations have recently been carried out on both bulk and interfacial systems[66-69,154,156]. The results of these studies have challenged the conventional view of the structure of both bulk and interfacial water. The XAS results on bulk liquid water has produced a picture of a first solvation shell that remains controversial[66,67]. Studies of liquid microjets consisting of neat water or methanol produced strong evidence for different types of surface water molecules at the liquid-vapor interfaces[68,69,154,156]. For the neat aqueous interface an "acceptor-only" surface moiety is proposed wherein both hydrogen atoms of a surface water molecule extend out of the liquid[69] as opposed to the well recognized "single-donor" water for which only one hydrogen is dangling[157-161,170]. This finding is qualitatively different from earlier surface descriptions based on data obtained from SFG experiments. However, the sensitivity of this particular measurement to distinguish between acceptor-only and single-donor species may not be adequate[157]. The XAS measurements are sensitive to the precise nature of the solvating environment around a reference oxygen, whereas the SFG signal is sensitive to changes in vibrational frequencies produced by different hydrogen bonding

environments.

Extended x-ray absorption fine structure (EXAFS) experiments were also used by Wilson *et al*[68] to characterize liquid-vapor interfaces of water and methanol. The most intriguing finding for these neat systems is an outward surface relaxation (expansion) of ~6% for the aqueous liquid-vapor interface whereas they find an inward relaxation (contraction) of ~5% was observed for the neat methanol interface[68,156]. This outward relaxation for water could be related to charge rearrangement due to the unsatisfied bonding in the vicinity of the interface.

	Percentage of acceptor-only surface water molecules @ 300 K
TIP4P [1]	12
TIP4P-fq [8]	13
TIP4P-pol [10,11]	7
BLYP[14] [15]	19
exp	N/A

Table 1: Comparison of the acceptor-only populations of various water models. Hydrogen bond parameters are identical to those found in Ref. [2]. The classical empirical interaction potentials were simulated with Monte Carlo utilizing 1600 atoms in a 30Åx30Åx100Å supercell.

In order to capture the fundamental physical chemistry revealed by the recent x-ray data[66,68,69,154-156], the inclusion of many-body polarization effects in an unbiased manner through the use of first-principles interaction potentials is thus imperative.

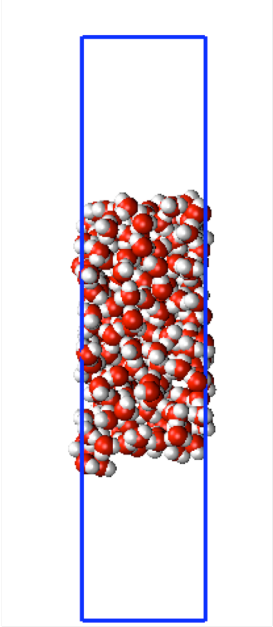

Figure 12: Side view (along *z*) of the supercell of the 216 water molecule aqueous liquid-vapor interface[2]. The supercell is superimposed in blue.

A first attempt at using KS-DFT based methods to elucidate the aqueous liquid-vapor interface was performed using 32 water molecules[171]. Although this study provided interesting observations of surface moieties, we can now look at the effects of small system size and boundary conditions can have on the outcome of this simulation. One can ask the question regarding the effects of system size and boundary conditions on the stability of a liquid vapor interface. Figure 10 shows the initial and finial configuration of 32 waters of a liquid-vapor interface using a full 3D periodic boundary conditions. As one can see, after 5 ps of MD, the final

configuration is not a stable liquid-vapor interface. The issue whether boundary conditions or system size can be addressed by performing the identical calculation with the 2D screening potential that was derived in section 2.3. The outcome of this simulation is depicted in Figure 11 and shows marked differences with Figure 10. In Figure 11 the interfaces are well defined and stabilized by the presence of the 2D-screening function, but there is a clear layering effect, presumably due to the lack of a stable bulk region within the 32 water liquid-vapor interface. Recall, that the simulations outlined in section 4 also contained on the order of 32 waters to describe the solid-vapor interfacial system. In these cases, one is able to constrain a layer to the bulk crystalline conditions in order to mimic interaction with a converged bulk material. Unfortunately, when simulating liquid-vapor interfaces, no such trick can be applied, and having a fully stabilized bulk region is imperative for a stable simulation. Thus, it is clear that *both* boundary conditions and system size will play a role in simulating a stable liquid-vapor interface.

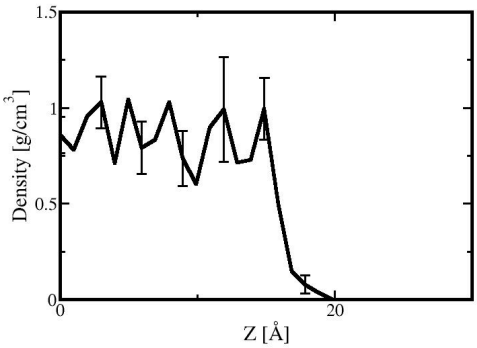

Figure 13: Density profile for the 216 water aqueous liquid-vapor interface[2]. Statistics were gathered over the last 4 ps of a 7 ps run.

Through the recent availability of tera-scale computing at Lawrence Livermore National Laboratory (LLNL) and the excellent scaling properties of **CPMD**[24,172], a stable aqueous liquid-vapor interface with first-principles interaction potentials is now possible[2,173]. This calculation was performed on 216 water molecules at 300K in a simulation cell of dimension 15 Å by 15 Å by 71.44 Å (see Figure 12). The decoupling of the periodic images

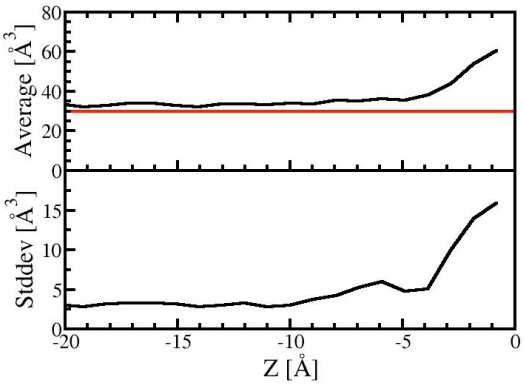

Figure 14: Plot of the Voronoi volumes (top) and their standard deviations (bottom) for the 216 water aqueous liquid –vapor interface[2]. The red horizontal line is at 29.9 Å^3/molecule indicating a density of 1 g/cm^3. Statistics were gathered over the last 4 ps of a 7 ps run.

was performed with methods outlined in section 2.3. The distance between the two free interfaces in the *z* direction was approximately 35 Å, indicating that there should be roughly 5 to 10 Å of bulk water. The initial configuration was obtained from classical molecular dynamics after an equilibration period of 100 ps at 300 K. After the initial wave function optimization, **CPMD** was performed for 7 ps. The simulation was performed on the 11 teraflop Multiprogrammatic Capability Resource (MCR) Linux cluster at LLNL (see http://www.top500.org) utilizing a total of 1440 CPUs[24,172]. The simulation parameters were chosen to ensure adiabaticity through out the MD simulation[2,9]. A Nosé-Hoover thermostat[139,140] was attached to every degree of freedom to ensure proper thermalization over the MD trajectory. This brute-force approach to thermostatting was needed to insure that a stable liquid-vapor interface was achieved. In principle, over a long enough trajectory, there will be a proper mixing of all the degrees of freedom to ensure that the entire interfacial system reaches the desired temperature. Because of the relatively short trajectories afforded by first-principles MD, without proper temperature control, there is the potential for the region in the vicinity of the interface to be significantly hotter than the corresponding bulk region.

CPMD/CP2K	Bulk	Interface
32 H_2O	0.130/0.041	0.262/0.047
64 H_2O	0.527/0.098	1.080/0.101
128 H_2O	2.739/0.3527	6.392/0.5927

Table 2**:** Extrapolated total number of CPU years that are required to generate a 10ps of trajectory using 0.097 fs timestep with a cutoff of 85Ry and 0.48 fs time-step with a density cutoff of 280Ry for **CPMD** and **CP2K**/QUICKSTEP benchmarks, respectively. The density for the bulk simulations was set at 1.0 g/ml while for the simulated interfacial systems, the length of the supercell in the *Z* direction was double to simulate the cost of a converged 2D periodic calculation. (detailed discussion in section 2.3). The amount of CPU years was extrapolated from a benchmark performed over 4 CPUs for the 32 and 64 H_2O test systems and 16 CPU for the 128 H_2O system where each CPU is an Intel Itanium2 running at 1.4GHz. The simulation parameter can be found else where[9].

The post-processing of the electronic structure was performed with **CP2K**[27] (see section 2.2) by averaging 15 configurations over the last 4 ps using the QUICKSTEP[43,45] package in conjunction with gradient corrected BLYP functional,[14,174] dual-space PPs[34], and a Triple Zeta plus Double Polarization (TZV2P) basis set

for the valence states. Table 2 gives the extrapolated CPU years for 10 ps trajectory using the methods discussed in sections 2.1 and 2.2. It is clear that the hybrid method discussed in section 2.2 performs very well for large, interfacial systems.

Before one can proceed with analyzing the liquid-vapor interface for novel hydrogen bonding moieties and reactivity, there must be some effort towards showing that one indeed has a stable interfacial system. This is most easily done with the computation of a density profile. Figure 13 depicts this profile, and it indeed suffers from lack of convergence. This is not due to a frozen interior region as can be gleaned from the examination of the orientational relaxation indicating that the librational peak for a hindered rotation is in good agreement with bulk studies[2]. The lack of smoothness can be explained by recalling that density profiles sample a discrete representation of space, and thus much longer trajectories are needed in order to obtain a smooth, converged density profile. We can also compute the volume of each individual water molecule as a function of its continuous spatial coordinate by utilizing Voronoi polyhedra[175,176]. This profile is depicted in Figure 14 along with the standard deviation of the volumes as a function of the interfacial coordinate. It is clear the Figure 13 and Figure 14 contain the same information. However, the salient feature of the Voronoi plot is that the signature of a stable bulk region is apparent when examining average volume/molecule as a function of the interfacial coordinate. Figure 14 also corroborates the result obtained by examining density profile in Figure 13, that the natural density of BLYP water may be less than 1 g/cm^3. One also observes that the standard deviation of the Voronoi volumes in Figure 14 begins to increase well before the Gibb's dividing surface, namely the point where the density is half of the bulk value. This is an indication that there may be surface relaxation in the vicinity of the liquid-vapor interface. Because even 7 ps (let alone the 1 ps trajectories reviewed in section 4.1) is not enough time to observe the identical average behavior of both free interfaces, all interfacial properties in this study are averaged over both free interfaces. To further corroborate the presence of surface relaxation, the average oxygen-oxygen distance in the bulk and interfacial regions can be computed using the minimum of the as a distance cut-

off (see Figure 15). The interior region of the interface has an average oxygen-oxygen distance of 2.93Å whereas it is 2.96Å in the vicinity of the interface. From this analysis, in addition to surface RDFs[2] that were computed, it is clear that there is a strong signature for a positive surface relaxation in interfacial in agreement with recent experiments[68].

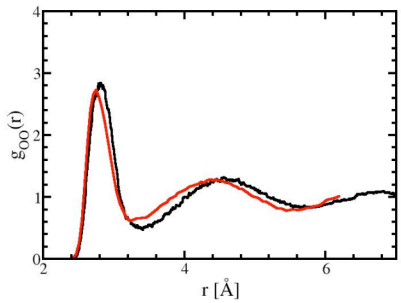

Figure 15: Oxygen-oxygen RDF (g_{OO}) of the interior of the 216 water aqueous liquid vapor interface[2] (red) and a 64 water bulk simulation of liquid water simulated under the conditions in Ref. [9] (black).

The effect of the density of the interior of the interfacial slab being less than 1 g/cm^3 is manifest in the RDFs shown in Figure 15. It is clear that the first peak is identical to a KS-DFT calculation of 64 waters at a fixed density of 1 g/cm^3, but the second solvation shell is shifted towards slightly higher values.

Given the usual caveats of system size and trajectory length, it is apparent that is possible to stabilize an aqueous liquid-vapor interface with a first-principles interaction potentials. It was alluded to earlier in this section that XAS experiments on interfacial water have detected the acceptor-only hydrogen bonding moiety. Given an MD trajectory, it is now possible to classify and count hydrogen bond populations at the interface. This procedure can be done using a reasonable definition of a hydrogen bond, and indeed, finite populations of both single-donor and acceptor-only moieties are present[2,173]. However, this should not come as a surprise, given that the configuration of the acceptor-only is not energetically forbidden, there will be some finite population. This is borne out in Table 1, where the acceptor-only populations are plotted for a variety of classical empirical potentials and compared to the first-principles data using the hydrogen bond definition in Ref [2]. Clearly the population of acceptor-only hydrogen bond populations is not dependent on the underlying model to represent water. It is of interest to note that the surface IR spectrum can also be computed yielding the distinctive peak at 3700 cm^{-1}.[2] Although this surface IR verifies the existence of dangling OH bonds at the liquid-vapor interface, it cannot distinguish between the acceptor-only and single-donor moieties. However, recent theoretical analysis of the SFG spectrum

have found a spectroscopic signature for the so-called surface "wagging"-mode which is analogous to the acceptor-only species[177].

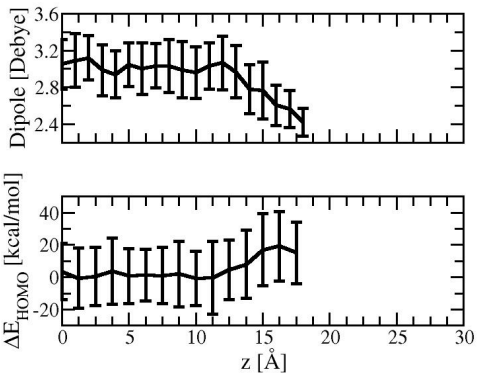

Figure 16: Dipole moment and molecular states of the 216 water aqueous liquid-vapor interface. Decrease in dipole moment as one approaches the interface was also found by Dang *et. al* using polarizable empirical interaction potentials.[4]

A first-principles trajectory also offers a glimpse into the reactivity of this important system. An analysis needs to be performed that allows one to look at the frontier orbitals (*i.e.* the highest occupied molecular orbital (HOMO) and lowest unoccupied molecular orbital (LUMO)) of a particular molecule as a function of the slab coordinate. Although the KS states will give us the frontier picture that we desire, there is no way of associating a particular electronic state with a molecule, and hence define its energy. In section 3.1 we describe a way of partitioning valence charge with the use of WFs[178,179]. Although WFs can be computed, they are not eigenfunctions of the H_{KS}, and thus cannot be used for a frontier analysis. However, we can project H_{KS} into the WF basis,

$$H_{\mathrm{WF}}^{ij} = \sum_{k} U_{ik}^{*} U_{jk} \, H_{KS}^{ij}$$

Eqn. 35

and re-diagonalize sub-blocks of H_{WF} containing the states that belong to a particular molecule (see Figure 5) to obtain eigenvalues for each molecule. These eigenvalues are the so-called molecular states and can be used to construct HOMOs of individual molecules as a function of their chemical environment (in this case the distance from the Gibb's dividing surface).

Using this methodology we can plot the HOMO and dipole moment (see section 3.1) of each water molecule in the aqueous liquid-vapor interface as a function of the interfacial coordinate. This is shown in Figure 16, and it indicates a trend toward higher reactivity and lower dipole moment as one

approaches the interfacial region. Last, Figure 17 depicts the HOMO and LUMO obtained via the KS states and shows for this particular snapshot that the interface is reactive to both excess protons and excess electrons corroborating the molecular states analysis.

6 Future prospects and applications

In summary, it is clear that the use of first-principles techniques for tackling the difficult problems associated with heterogeneous environments is an emerging area with immense potential. Atmospherically relevant interfaces (whether it be a PSC or aerosol) pose many unanswered questions pertaining to reactivity that are addressable with the use of the sophisticated models that have been reviewed here. It should now be clear to the reader that the new methods for electronic structure calculations, outlined in section 2, are well suited for accurate and efficient studies interfacial systems. Moreover, with the development and further use and testing of hybrid methods to solve electronic structure problems, researchers will not have to rely on supercomputing hardware that is only currently present at our National Laboratories. Having fast electronic structure software suites that are and publicly available should allow for rapid development of this important area of research.

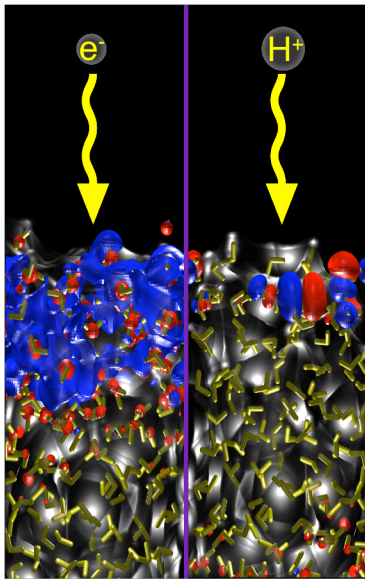

Figure 17: The KS HOMO (left) and LUMO (right) of the 216 water aqueous liquid-vapor interface[2]. The results indicate that the aqueous surface is reactive to both excess protons and electrons.

However, one common thread that is true amongst all of the studies performed in this review is the careful examination of the theoretical findings in the framework of experiment. Another commonality was the inability to pin down a precise reaction mechanism within a dynamical framework (with the exception of the mechanism for Cl_2 formation put forth in section 4.1). This is most likely due to the role of complicated intermediate states, as well as the precise role of the interface that is postulated to undergo significant structural changes during a reaction. Both of these issues conspire in a way to make

the sampling of these unknown reaction pathways extremely difficult, if not computationally prohibitive. Thus, in closing we will offer a *preview,* rather than a *review* of the application of a technique to sample complex multidimensional reaction coordinates, that when combined with the methods outlined in section 2, could make the study of reaction mechanisms that take place in the vicinity of an interface, tractable with the use of first-principles interaction potentials.

6.1 Metadynamics

It is known that MD simulation is very inefficient in sampling free energy surface (FES), $V(\mathbf{r})$, due to the limited simulation time and high-energy barriers. Moreover, first-principles simulations suffer even more, because the computational cost is even higher. This is very problematic since one of the main advantages of using first-principles interaction potentials over classical empirical potentials is the ability to look at bond formation. One common method for addressing the time-scale issue for sampling FES with high energy barriers between local minima is through the use of umbrella sampling in conjunction with constrained MD[180-182]. In an umbrella sampling scheme, one first needs to identify a reasonable reaction coordinate to sample. Once the reaction coordinate is chosen, constrained MD is performed at regular intervals along the reaction coordinate yielding N independent simulations. The weighted population from the constrained MD simulation is then pieced together using weighed histogram analysis method (WHAM).[180-182]

Though an umbrella sampling scheme in conjunction with WHAM, a FES can be constructed. However, there are drawbacks to using such a procedure. In particular for a given system where a single one-dimensional reaction coordinate is known, N multiple independent simulations must be carried out using a biasing potential spaced out equally along the reaction coordinate. In the case where the reaction coordinate and FES must be described in two dimensions, then N^2 independent simulations must be carried out. To alleviate the unfavorable scaling of umbrella sampling with the underlying complexity of the FES, a new variation of umbrella sampling has been proposed by Laio *et. al.*[183,184]

called *metadynamics*. *Metadynamics* is similar to the traditional umbrella sampling scheme outlined above with the exception that the biasing potential are not fixed but can self-adapt over the course of the simulation. Like an umbrella sampling scheme, a *metadynamics* simulation is carried out first by assuming that there are a finite number of relevant collective coordinates, $s_i(\mathbf{r})$, for any FES where ($i = 1,n$). The only restriction on the choice of collective coordinates that the must be derivable with respect to $\mathbf{r}$. It is common to express the collective variables as a distance, angle, or even coordination number with respect to a particular atom[7,185-191]. Once the relevant collective variables and coordinates are chosen, normal MD simulations are carried out where the evolution of the system evolves on the potential $V_{\text{ext}}(\mathbf{r},t)$ as described in section 2.1 where the potential is now time dependent with the form

$$V_{\text{ext}}(\mathbf{r},t) = V_{\text{FES}}(\mathbf{r}) + V_{\text{meta}}(s,t)$$

Eqn. 36

where at $t = 0$, the time dependent term $V_{\text{meta}}(s,t) = 0$. Once there is an adequate amount of sampling of the local FES, an additional potential is added to bias the trajectory away from the present landscape, namely,

$$V_{\text{meta}}(s,t) = \sum_t W \exp\left(-\frac{|\sigma - \sigma'|^2}{2\delta\sigma^2}\right).$$

Eqn. 37

Though this biasing potential can be of any form, Gaussians are chosen because of its ease of implementation and derivability with respect to the height and width (W and $\delta\sigma$ respectively) which are parameters which alter the accuracy and efficiency of how one samples the FES. As the simulation proceeds, the aforementioned procedure is repeated and $V_{\text{ext}}(\mathbf{r},t)$ evolves according to $V_{\text{meta}}(s,t)$. Eventually the biasing potential, $V_{\text{meta}}(s,t)$ will converge to the negative of the actual FES.

A simple example of a *metadynamics* simulation based on first-principles MD simulation is shown in Figure 18 where we attempt to map out the FES for the internal proton transfer of malonaldehyde analogous to the work of Tuckerman and Marx.[192] Tuckerman and Marx found that within the classical approximation at 300K, the energy barrier between proton transfer was roughly 3.5 kcal/mol. Here, using very modest computational resources ($N_{CPU} < 16$) we were able to reproduce the FES with error commensurate to the choices of height and width (W and $\delta\sigma$ respectively) using a single simulation utilizing *metadynamics*. For more complex systems, *metadynamics* has also been shown to generate equivalent FES when compared to umbrella sampling[191]. Other sources of information is available for a recipe and discussion on the optimal selection of W and $\delta\sigma$ to reduce error and maximize computational efficiencies.[185,186]

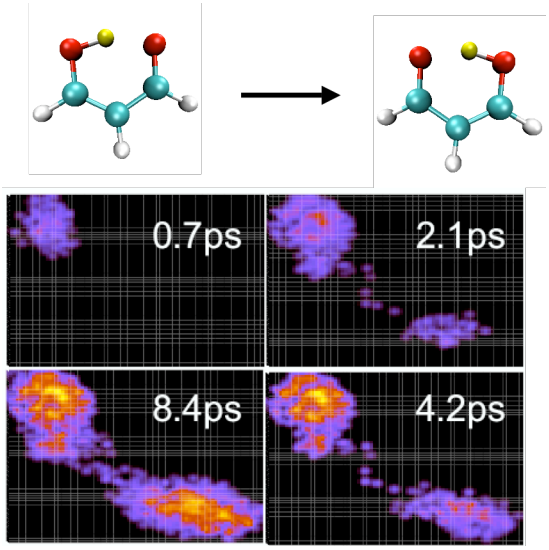

Figure 18 The evolution of the two dimensional FES for the intermolecular proton transfer in malonaldehyde (top, oxygen in red, carbon in green, hydrogen, white and the transferring proton in yellow) from a first-principles MD simulation where the metadynamics algorithm is used to map out the FES and the transition state. Here we used a the coordination number constraint on the two oxygens[7] thus forcing the proton (yellow) to sample the two free-energy basins over time.

7 Acknowledgments

We thank Larry Fried and Charlie Westbrook for their ongoing support of this work. This work was performed under the auspices of the U.S. Department of Energy by the University of California Lawrence Livermore National Laboratory (LLNL) under contract No. W-7405-Eng-48. Computer resources were provided by the Livermore Computing.

8 References

(1) Jorgensen, W. L.; Chandrasekhar, J.; Madura, J.; Impey, R. W.; Klein, M. L. *Journal of Chemical Physics* **1983**, *79*, 926-935.
(2) Kuo, I. F. W.; Mundy, C. J. *Science* **2004**, *303*, 658-660.
(3) Casassa, S.; Pisani, C. *Journal Of Chemical Physics* **2002**, *116*, 9856-9864.
(4) Dang, L. X.; Chang, T. M. *Journal of Chemical Physics* **1997**, *106*, 8149-8159.
(5) Lee, S. H.; Leard, D. C.; Zhang, R. Y.; Molina, L. T.; Molina, M. J. *Chemical Physics Letters* **1999**, *315*, 7-11.
(6) Mantz, Y. A.; Geiger, F. M.; Molina, L. T.; Molina, M. J.; Trout, B. L. *Chemical Physics Letters* **2001**, *348*, 285-292.
(7) Stirling, A.; Iannuzzi, M.; Laio, A.; Parrinello, M. *Chemphyschem* **2004**, *5*, 1558-1568.
(8) Rick, S. W.; Stuart, S. J.; Berne, B. J. *Journal of Chemical Physics* **1994**, *101*, 6141-6156.
(9) Kuo, I. F. W.; Mundy, C. J.; McGrath, M. J.; Siepmann, J. I.; VandeVondele, J.; Sprik, M.; Hutter, J.; Chen, B.; Klein, M. L.; Mohamed, F.; Krack, M.; Parrinello, M. *J. Phys. Chem. B* **2004**, *108*, 12990-12998.
(10) Chen, B.; Xing, J. H.; Siepmann, J. I. *Journal of Physical Chemistry B* **2000**, *104*, 2391-2401.
(11) Molina, M. J. *Angew. Chem. Int. Edit.* **1996**, *35*, 1778-1785.
(12) Knipping, E. M.; Lakin, M. J.; Foster, K. L.; Jungwirth, P.; Tobias, D. J.; Gerber, R. B.; Dabdub, D.; Finlayson-Pitts, B. J. *Science* **2000**, *288*, 301.
(13) Laskin, A.; Gaspar, D. J.; Wang, W. H.; Hunt, S. W.; Cowin, J. P.; Colson, S. D.; Finlayson-Pitts, B. J. *Science* **2003**, *301*, 340-344.
(14) Becke, A. D. *Physical Review A* **1988**, *38*, 3098.
(15) Lee, C.; Yang, W.; Parr, R. G. *Physical Review B (Condensed Matter)* **1988**, *37*, 785-9.
(16) Rowland, F. S. *Angew. Chem. Int. Edit.* **1996**, *35*, 1786-1798.
(17) Dang, L. X.; Smith, D. E. *Journal of Chemical Physics* **1993**, *99*, 6950-6956.
(18) Car, R.; Parrinello, M. *Phys. Rev. Lett.* **1985**, *55*, 2471.
(19) Hohenberg, P.; Kohn, W. *Physical Review* **1964**, *136*, B86.
(20) Kohn, W.; Sham, L. A. *Physical Review A* **1965**, *140*, 1133.
(21) Parr, R. G.; Yang, W. *Density-functional theory of atoms and molecules*; Oxford University Press; Clarendon Press: New York, 1989.
(22) HeadGordon, M. *Journal of Physical Chemistry* **1996**, *100*, 13213-13225.
(23) Kohn, W.; Becke, A. D.; Parr, R. G. *J. Phys. Chem.* **1996**, *100*, 12974-12980.
(24) Marx, D.; Hutter, J. In *Modern Methods and Algorithms of Quantum Chemistry*; Grotendorst, J., Ed.; John von Neumann Institute for Computing: Forschungszentrum Julich, 2000; Vol. 1.
(25) Grossman, J. C.; Schwegler, E.; Draeger, E. W.; Gygi, F.; Galli, G. *Journal of Chemical Physics* **2004**, *120*, 300-311.
(26) Schwegler, E.; Grossman, J. C.; Gygi, F.; Galli, G. *Journal of Chemical Physics* **2004**, *121*, 5400-5409.
(27) CP2K.
(28) CPMD.
(29) Dovesi, R.; Saunders, V. R.; Roetti, C.; Causa, N.; Harrison, N. M.; Orlando, R.; Apra, E. *CRYSTAL95 User's Manual*; Universita di Torino: Torino, 1996.
(30) Pisani, C.; Cora, F.; Nada, R.; Orlando, R. *Computational Physics Communications* **1994**, *82*, 139.
(31) Pisani, C.; Dovesi, R.; Roetti, C. *Hartree-Fock Ab Initio Treatment of Crystalline Systems*; Springer: Berlin, 1988.
(32) Hutter, J.; Ballone, P.; Bernasconi, M.; Focher, P.; Fois, E.; Goedecker, S.; Parrinello, M.; Tuckerman, M. E. *CPMD code, version 3.3*; MPI fuer Festkoerperforschung, Stuttgart and IBM Zurich Research Laboratory, 1990-1996.
(33) Troullier, N.; Martins, J. L. *Phys. Rev. B* **1991**, *43*, 1993.

(34) Goedecker, S.; Teter, M.; Hutter, J. *Physical Review B* **1996**, *54*, 1703.
(35) Vanderbilt, D. *Physical Review B* **1990**, *41*, 7892-7895.
(36) Perdew, J. P.; Burke, K.; Ernzerhof, M. *Physical Review Letters* **1996**, *77*, 3865-3868.
(37) Hamprecht, F. A.; Cohen, A. J.; Tozer, D. J.; Handy, N. C. *Journal of Chemical Physics* **1998**, *109*, 6264-6271.
(38) Handy, N. C.; Cohen, A. J. *Journal of Chemical Physics* **2002**, *116*, 5411-5418.
(39) Becke, A. D. *Journal of Chemical Physics* **1993**, *98*, 5648.
(40) Adamo, C.; Barone, V. *Journal of Chemical Physics* **1999**, *110*, 6158-6170.
(41) Xu, X.; Goddard, W. a. *Proceedings of the National Academy of Sciences of the United States of America* **2004**, *101*, 2673-2677.
(42) Press, W. H. *Numerical recipes in C: the art of scientific computing*; 2nd, rev. ed.; Cambridge University Press: Cambridge Cambridgeshire; New York, 1997.
(43) Lippert, G.; Hutter, J.; Parrinello, M. *Mol. Phys.* **1997**, *92*, 477.
(44) Lippert, G.; Hutter, J.; Parrinello, M. *Theoretical Chemistry Accounts* **1999**, *103*, 124-140.
(45) VandeVondele, J.; Krack, M.; Mohamed, F.; Parrinello, M.; Chassaing, T.; Hutter, R. *Computer Physics Communications* **2005**, *167*, 103-128.
(46) VandeVondele, J.; Mohamed, F.; Krack, M.; Hutter, J.; Sprik, M.; Parrinello, M. *Journal of Chemical Physics* **2005**, *122*, -.
(47) Jensen, F. *Introduction to computational chemistry*; Wiley: Chichester; New York, 1999.
(48) Darden, T.; York, D.; Pedersen, L. *Journal of Chemical Physics* **1993**, *98*, 10089-10092.
(49) Hockney, R. W. *Methods in Computational Physics* **1970**, *9*, 136.
(50) Martyna, G. J.; Tuckerman, M. E. *J. Chem. Phys.* **1999**, *110*, 2810-2821.
(51) Mortensen, J. J.; Parrinello, M. *Journal Of Physical Chemistry B* **2000**, *104*, 2901-2907.
(52) Minary, P.; Tuckerman, M. E. *Journal Of The American Chemical Society* **2005**, *127*, 1110-1111.
(53) Barnett, R. N.; Landman, U. *Physical Review B* **1993**, *48*, 2081-2097.
(54) Morita, A.; Hynes, J. T. *Chem. Phys.* **2000**, *258*, 371.
(55) Morita, A.; Hynes, J. T. *J. Phys. Chem. B* **2002**, *106*, 673.
(56) Perry, A.; Ahlborn, H.; Space, B.; Moore, P. B. *Journal Of Chemical Physics* **2003**, *118*, 8411-8419.
(57) Silvestrelli, P. L.; Bernasconi, M.; Parrinello, M. *Chem. Phys. Lett.* **1997**, *277*, 478.
(58) Kingsmith, R. D.; Vanderbilt, D. *Phys. Rev. B* **1993**, *47*, 1651-1654.
(59) Marzari, N.; Vanderbilt, D. *Phys. Rev. B* **1997**, *56*, 12847-12865.
(60) Berghold, G.; Mundy, C. J.; Romero, A. H.; Hutter, J.; Parrinello, M. *Physical Review B* **2000**, *61*, 10040-10048.
(61) Silvestrelli, P. L.; Marzari, N.; Vanderbilt, D.; Parrinello, M. *Solid State Commun.* **1998**, *107*, 7.
(62) Putrino, A.; Sebastiani, D.; Parrinello, M. *Journal of Chemical Physics* **2000**, *113*, 7102-7109.
(63) Putrino, A.; Parrinello, M. *Physical Review Letters* **2002**, *88*, -.
(64) Borysow, J.; Moraldi, M.; Frommhold, L. *Molecular Physics* **1985**, *56*, 913-922.
(65) Berne, B. J.; Pecora, R. *Dynamic light scattering: with applications to chemistry, biology, and physics*; R.E. Krieger Pub. Co.: Malabar, Fla., 1990.
(66) Wernet, P.; Nordlund, D.; Bergmann, U.; Cavalleri, M.; Odelius, M.; Ogasawara, H.; Naslund, L. A.; Hirsch, T. K.; Ojamae, L.; Glatzel, P.; Pettersson, L. G. M.; Nilsson, A. *Science* **2004**, *304*, 995-999.
(67) Smith, J. D.; Cappa, C. D.; Wilson, K. R.; Messer, B. M.; Cohen, R. C.; Saykally, R. J. *Science* **2004**, *306*, 851-853.
(68) Wilson, K. R.; Schaller, R. D.; Co, D. T.; Saykally, R. J.; Rude, B. S.; Catalano, T.; Bozek, J. D. *J. Chem. Phys.* **2002**, *117*, 7738.
(69) Wilson, K. R.; Cavalleri, M.; Rude, B. S.; Schaller, R. D.; Nilsson, A.; Pettersson, L. G. M.; Goldman, N.; Catalano, T.; Bozek, J. D.; Saykally, R. J. *J. Phys. Condens. Mat.* **2002**, *14*, L221.
(70) Myneni, S.; Luo, Y.; Naslund, L. A.; Cavalleri, M.; Ojamae, L.; Ogasawara, H.; Pelmenschikov,

A.; Wernet, P.; Vaterlein, P.; Heske, C.; Hussain, Z.; Pettersson, L. G. M.; Nilsson, A. *J. Phys. Condens. Mat.* **2002**, *14*, L213.
(71) Cavalleri, M.; Odelius, M.; Nilsson, A.; Pettersson, L. G. M. *Journal of Chemical Physics* **2004**, *121*, 10065-10075.
(72) Triguero, L.; Pettersson, L. G. M.; Agren, H. *Physical Review B* **1998**, *58*, 8097-8110.
(73) Triguero, L.; Pettersson, L. G. M.; Agren, H. *Journal of Physical Chemistry A* **1998**, *102*, 10599-10607.
(74) Hetenyi, B.; De Angelis, F.; Giannozzi, P.; Car, R. *Journal of Chemical Physics* **2001**, *115*, 5791-5795.
(75) Hetenyi, B.; De Angelis, F.; Giannozzi, P.; Car, R. *Journal of Chemical Physics* **2004**, *120*, 8632-8637.
(76) Bussolin, G.; Casassa, S.; Pisani, C.; Ugliengo, P. *Journal Of Chemical Physics* **1998**, *108*, 9516-9528.
(77) Casassa, S. *Chemical Physics Letters* **2000**, *321*, 1-7.
(78) Casassa, S.; Ugliengo, P.; Pisani, C. *Journal Of Chemical Physics* **1997**, *106*, 8030-8040.
(79) Liu, Z. F.; Siu, C. K.; Tse, J. S. *Chemical Physics Letters* **1999**, *309*, 335-343.
(80) Mantz, Y. A.; Geiger, F. M.; Molina, L. T.; Molina, M. J.; Trout, B. L. *Journal Of Chemical Physics* **2000**, *113*, 10733-10743.
(81) Mantz, Y. A.; Geiger, F. M.; Molina, L. T.; Molina, M. J.; Trout, B. L. *Journal Of Physical Chemistry A* **2002**, *106*, 6972-6981.
(82) Mantz, Y. A.; Geiger, F. M.; Molina, L. T.; Trout, B. L. *Journal Of Physical Chemistry A* **2001**, *105*, 7037-7046.
(83) Poshusta, R. D.; Tseng, D. C.; Hess, A. C.; McCarthy, M. I. *Journal Of Physical Chemistry* **1993**, *97*, 7295-7303.
(84) Svanberg, M.; Pettersson, J. B. C.; Bolton, K. *Journal Of Physical Chemistry A* **2000**, *104*, 5787-5798.
(85) Toth, G. *Journal Of Physical Chemistry A* **1997**, *101*, 8871-8876.
(86) Cicerone, R. J. *Science* **1987**, *237*, 35-42.
(87) Molina, M. J.; Tso, T. L.; Molina, L. T.; Wang, F. C. Y. *Science* **1987**, *238*, 1253-1257.
(88) Solomon, S.; Garcia, R. R.; Rowland, F. S.; Wuebbles, D. J. *Nature* **1986**, *321*, 755-758.
(89) Tolbert, M. A.; Rossi, M. J.; Golden, D. M. *Science* **1988**, *240*, 1018-1021.
(90) Tolbert, M. A.; Rossi, M. J.; Malhotra, R.; Golden, D. M. *Science* **1987**, *238*, 1258-1260.
(91) Gertner, B. J.; Hynes, J. T. *Science* **1996**, *271*, 1563-1566.
(92) Gertner, B. J.; Hynes, J. T. *Faraday Discussions* **1998**, 301-322.
(93) Bianco, R.; Gertner, B. J.; Hynes, J. T. *Berichte Der Bunsen-Gesellschaft-Physical Chemistry Chemical Physics* **1998**, *102*, 518-526.
(94) Bianco, R.; Hynes, J. T. *Journal Of Physical Chemistry A* **1998**, *102*, 309-314.
(95) Bianco, R.; Hynes, J. T. *International Journal Of Quantum Chemistry* **1999**, *75*, 683-692.
(96) Bianco, R.; Hynes, J. T. *Journal Of Physical Chemistry A* **1999**, *103*, 3797-3801.
(97) Bianco, R.; Hynes, J. T. *Journal of Physical Chemistry A* **2003**, *107*, 5253-5257.
(98) Bianco, R.; Thompson, W. H.; Morita, A.; Hynes, J. T. *Journal Of Physical Chemistry A* **2001**, *105*, 3132-3139.
(99) Bolton, K. *Journal Of Molecular Structure-Theochem* **2003**, *632*, 145-156.
(100) Bolton, K.; Pettersson, J. B. C. *Journal Of The American Chemical Society* **2001**, *123*, 7360-7363.
(101) Bournel, F.; Mangeney, C.; Tronc, M.; Laffon, C.; Parent, P. *Physical Review B* **2002**, *65*.
(102) Devlin, J. P.; Uras, N.; Sadlej, J.; Buch, V. *Nature* **2002**, *417*, 269-271.
(103) Graham, J. D.; Roberts, J. T. *Journal Of Physical Chemistry* **1994**, *98*, 5974-5983.
(104) Graham, J. D.; Roberts, J. T. *Geophysical Research Letters* **1995**, *22*, 251-254.
(105) Horn, A. B.; Sodeau, J. R.; Roddis, T. B.; Williams, N. A. *Journal Of Physical Chemistry A* **1998**, *102*, 6107-6120.

(106) Kang, H.; Shin, T. H.; Park, S. C.; Kim, I. K.; Han, S. J. *Journal Of The American Chemical Society* **2000**, *122*, 9842-9843.
(107) Milet, A.; Struniewicz, C.; Moszynski, R.; Sadlej, J.; Kisiel, Z.; Bialkowska-Jaworska, E.; Pszczolkowski, L. *Chemical Physics* **2001**, *271*, 267-282.
(108) Re, S.; Osamura, Y.; Suzuki, Y.; Schaefer, H. F. *Journal Of Chemical Physics* **1998**, *109*, 973-977.
(109) Shevkunov, S. V. *Colloid Journal* **2004**, *66*, 506-516.
(110) Shevkunov, S. V. *Colloid Journal* **2004**, *66*, 216-229.
(111) Toubin, C.; Picaud, S.; Hoang, P. N. M.; Girardet, C.; Demirdjian, B.; Ferry, D.; Suzanne, J. *Journal Of Chemical Physics* **2002**, *116*, 5150-5157.
(112) Xu, S. C. *Journal Of Chemical Physics* **1999**, *111*, 2242-2254.
(113) Banham, S. F.; Sodeau, J. R.; Horn, A. B.; McCoustra, M. R. S.; Chesters, M. A. *Journal Of Vacuum Science & Technology A-Vacuum Surfaces And Films* **1996**, *14*, 1620-1626.
(114) Donsig, H. A.; Herridge, D.; Vickerman, J. C. *Journal Of Physical Chemistry A* **1999**, *103*, 9211-9220.
(115) Donsig, H. A.; Vickerman, J. C. *Journal Of The Chemical Society-Faraday Transactions* **1997**, *93*, 2755-2761.
(116) Pursell, C. J.; Zaidi, M.; Thompson, A.; Fraser-Gaston, C.; Vela, E. *Journal Of Physical Chemistry A* **2000**, *104*, 552-556.
(117) Ando, K.; Hynes, J. T. In *Advances In Chemical Physics*, 1999; Vol. 110.
(118) Leu, M. T.; Timonen, R. S.; Keyser, L. F. *Journal Of Physical Chemistry A* **1997**, *101*, 278-282.
(119) Parent, P.; Laffon, C. *Journal Of Physical Chemistry B* **2005**, *109*, 1547-1553.
(120) Andersson, P. U.; Nagard, M. B.; Pettersson, J. B. C. *Journal Of Physical Chemistry B* **2000**, *104*, 1596-1601.
(121) Sadtchenko, V.; Giese, C. F.; Gentry, W. R. *Journal Of Physical Chemistry B* **2000**, *104*, 9421-9429.
(122) Uras, N.; Rahman, M.; Devlin, J. P. *Journal Of Physical Chemistry B* **1998**, *102*, 9375-9377.
(123) Furukawa, Y.; Nada, H. *Journal Of Physical Chemistry B* **1997**, *101*, 6167-6170.
(124) Furukawa, Y.; Yamamoto, M.; Kuroda, T. *Journal Of Crystal Growth* **1987**, *82*, 665-677.
(125) Karim, O. A.; Haymet, A. D. J. *Chemical Physics Letters* **1987**, *138*, 531-534.
(126) Karim, O. A.; Haymet, A. D. J. *Journal Of Chemical Physics* **1988**, *89*, 6889-6896.
(127) Nada, H.; Furukawa, Y. *Applied Surface Science* **1997**, *121*, 445-447.
(128) Nada, H.; Furukawa, Y. *Surface Science* **2000**, *446*, 1-16.
(129) Shevkunov, S. V. *Colloid Journal* **2004**, *66*, 230-238.
(130) Petrenko, V. F.; Whitworth, R. W. *Physics of Ice*; Oxford University Press: New York, 1999.
(131) Bullemer, B.; Riehl, N. *Solid State Communications* **1966**, *4*, 447-&.
(132) Dosch, H.; Lied, A.; Bilgram, J. H. *Surface Science* **1995**, *327*, 145-164.
(133) Gilpin, R. R. *Journal Of Colloid And Interface Science* **1980**, *77*, 435-448.
(134) Golecki, I.; Jaccard, C. *Journal Of Physics C-Solid State Physics* **1978**, *11*, 4229-4237.
(135) Mazzega, E.; Pennino, U. D.; Loria, A.; Mantovani, S. *Journal Of Chemical Physics* **1976**, *64*, 1028-1031.
(136) Mizuno, Y.; Hanafusa, N. *Journal De Physique* **1987**, *48*, 511-517.
(137) Nason, D.; Fletcher, N. H. *Journal Of Chemical Physics* **1975**, *62*, 4444-4449.
(138) Abbatt, J. P. D.; Molina, M. J. *Journal Of Physical Chemistry* **1992**, *96*, 7674-7679.
(139) Hoover, W. G. *Physical Review A* **1985**, *31*, 1695.
(140) Nose, S. *J. Chem. Phys.* **1984**, *81*, 511-519.
(141) Kroes, G. J. *Surface Science* **1992**, *275*, 365-382.
(142) Allouche, A.; Couturier-Tamburelli, I.; Chiavassa, T. *Journal Of Physical Chemistry B* **2000**, *104*, 1497-1506.
(143) Schaff, J. E.; Roberts, J. T. *Journal Of Physical Chemistry* **1994**, *98*, 6900-6902.
(144) Kresse, G.; Hafner, J. *Physical Review B* **1993**, *47*, 558-561.

(145) Kresse, G.; Hafner, J. *Physical Review B* **1994**, *49*, 14251-14269.
(146) Laasonen, K.; Sprik, M.; Parrinello, M.; Car, R. *Journal of Chemical Physics* **1993**, *99*, 9080-9089.
(147) Sprik, M.; Hutter, J.; Parrinello, M. *Journal of Chemical Physics* **1996**, *V105*, 1142-1152.
(148) Asthagiri, D.; Pratt, L. R.; Kress, J. D. *Physical Review E* **2003**, *68*.
(149) Sullivan, D. M.; Bagchi, K.; Tuckerman, M. E.; Klein, M. L. *Journal Of Physical Chemistry A* **1999**, *103*, 8678-8683.
(150) Finlayson-Pitts, B. J. *Chemical Reviews* **2003**, *103*, 4801-4822.
(151) Vieceli, J.; Roeselova, M.; Tobias, D. J. *Chemical Physics Letters* **2004**, *393*, 249-255.
(152) Chuang, P. Y.; Charlson, R. J.; Seinfeld, J. H. *Nature* **1997**, *390*, 594-596.
(153) Morita, A.; Sugiyama, M.; Kameda, H.; Koda, S.; Hanson, D. R. *Journal of Physical Chemistry B* **2004**, *108*, 9111-9120.
(154) Wilson, K. R.; Tobin, J. G.; Ankudinov, A. L.; Rehr, J. J.; Saykally, R. J. *Phys. Rev. Lett.* **2000**, *85*, 4289.
(155) Wilson, K. R.; Rude, B. S.; Schaller, R. D.; Catalano, T.; Saykally, R. J.; Cavalleri, M.; Pettersson, L. G. M.; Nilsson, A. *Journal of Physical Chemistry B* **2004**, *(in press)*.
(156) Wilson, K. R.; Rude, B. S.; Catalano, T.; Schaller, R. D.; Tobin, J. G.; Co, D. T.; Saykally, R. J. *J. Phys. Chem. B* **2001**, *105*, 3346.
(157) Richmond, G. L. *Chemical Reviews* **2002**, *102*, 2693-2724.
(158) Raymond, E. A.; Richmond, G. L. *Journal of Physical Chemistry B* **2004**, *108*, 5051-5059.
(159) Raymond, E. A.; Tarbuck, T. L.; Brown, M. G.; Richmond, G. L. *J. Phys. Chem. B* **2003**, *107*, 546.
(160) Allen, H. C.; Raymond, E. A.; Richmond, G. L. *Current Opinion in Colloid & Interface Science* **2000**, *5*, 74-80.
(161) Du, Q.; Superfine, R.; Freysz, E.; Shen, Y. R. *Physical Review Letters* **1993**, *70*, 2313.
(162) Schnitzer, C.; Baldelli, S.; Campbell, D. J.; Shultz, M. J. *Journal of Physical Chemistry* **1999**, *103*, 6383-6386.
(163) Schnitzer, C.; Baldelli, S.; Shultz, M. J. *J. Phys. Chem. B* **2000**, *104*, 585-590.
(164) Liu, D. F.; Ma, G.; Levering, L. M.; Allen, H. C. *Journal of Physical Chemistry B* **2004**, *108*, 2252-2260.
(165) Townsend, R. M.; Gryko, J.; Rice, S. A. *Journal of Chemical Physics* **1985**, *82*, 4391-4392.
(166) Townsend, R. M.; Rice, S. A. *Journal of Chemical Physics* **1991**, *94*, 2207-2218.
(167) Wilson, M. A.; Pohorille, A.; Pratt, L. R. *J. Phys. Chem.* **1987**, *91*, 4873.
(168) Benjamin, I. *Journal of Chemical Physics* **1991**, *95*, 3698-3709.
(169) Benjamin, I. *Physical Review Letters* **1994**, *73*, 2083.
(170) Schnitzer, C.; Baldelli, S.; Shultz, M. J. *Chemical Physics Letters* **1999**, *313*, 416-420.
(171) Vassilev, P.; Hartnig, C.; Koper, M. T. M.; Frechard, F.; van Santen, R. A. *J. Chem. Phys.* **2001**, *115*, 9815.
(172) Hutter, J.; Alavi, A.; Deutsch, T.; Bernasconi, M.; Goedecker, S.; Marx, D.; Tuckerman, M.; Parrinello, M.; 3.3a ed.; CPMD Program, MPI fur Festkorperforschung and IBM Zurich Research Laboratory, 1995-1999.
(173) Marx, D. *Science* **2004**, *303*, 634-636.
(174) Lee, C.; Yang, W.; Parr, R. G. *Phys. Rev. B* **1988**, *37*, 785.
(175) Gerstein, M.; Tsai, J.; Levitt, M. *J. Mol. Biol.* **1995**, *249*, 955.
(176) Harpaz, Y.; Gerstein, M.; Chothia, C. *Structure* **1994**, *2*, 641.
(177) Perry, A.; Niepert, C.; Ridley, C.; Space, B.; Moore, P. *Physical Review E*, *71*, 050601(R).
(178) Hunt, P.; Sprik, M.; Vuilleumier, R. *Chemical Physics Letters* **2003**, *376*, 68.
(179) Vuilleumier, R.; Sprik, M. *J. Chem. Phys.* **2001**, *115*, 3454-3468.
(180) Kumar, S.; Bouzida, D.; Swendsen, R. H.; Kollman, P. a.; Rosenberg, J. M. *Journal of Computational Chemistry* **1992**, *13*, 1011-1021.
(181) Kumar, S.; Rosenberg, J. M.; Bouzida, D.; Swendsen, R. H.; Kollman, P. a. *Journal of*

Computational Chemistry **1995**, *16*, 1339-1350.
(182) Souaille, M.; Roux, B. *Computer Physics Communications* **2001**, *135*, 40-57.
(183) Laio, A.; Parrinello, M. *Proceedings of the National Academy of Sciences of the United States of America* **2002**, *99*, 12562-12566.
(184) Iannuzzi, M.; Laio, A.; Parrinello, M. *Physical Review Letters* **2003**, *90*.
(185) Laio, a.; Rodriguez-Fortea, A.; Gervasio, F. L.; Ceccarelli, M.; Parrinello, M. *Journal of Physical Chemistry B* **2005**, *109*, 6714-6721.
(186) Ensing, B.; Laio, A.; Parrinello, M.; Klein, M. L. *Journal of Physical Chemistry B* **2005**, *109*, 6676-6687.
(187) Stirling, A.; Iannuzzi, M.; Parrinello, M.; Molnar, F.; Bernhart, V.; Luinstra, G. A. *Organometallics* **2005**, *24*, 2533-2537.
(188) Gervasio, F. L.; Laio, A.; Iannuzzi, M.; Parrinello, M. *Chemistry-A European Journal* **2004**, *10*, 4846-4852.
(189) Churakov, S. V.; Iannuzzi, M.; Parrinello, M. *Journal Of Physical Chemistry B* **2004**, *108*, 11567-11574.
(190) Iannuzzi, M.; Parrinello, M. *Physical Review Letters* **2004**, *93*.
(191) Gervasio, F. L.; Laio, A.; Parrinello, M. *Journal Of The American Chemical Society* **2005**, *127*, 2600-2607.
(192) Tuckerman, M. E.; Marx, D. *Physical Review Letters* **2001**, *86*, 4946-4949.